

Technical Report – TR29

Version 1.0 25 July 2003

Met Office Observations Development (OD)



Radiometrics MP3000 Microwave Radiometer Performance Assessment

Version 1.0
25 July 2003

Tim Hewison

Catherine Gaffard

Met Office
University of Reading, Meteorology Building
PO Box 243, Earley Gate, Reading
RG6 6BB, UK

Tel: +44 (0)118 378 7830
Fax: +44 (0)118 378 8791
E-mail: tim.hewison@metoffice.com



Contents

1. Executive Summary	3
2. Introduction	4
3. Description of Radiometer	5
Microwave Window.....	5
Antenna.....	6
The Microwave Receivers	6
Channel Frequencies	7
Observation Cycle	8
Tip Curve Calibrations	10
Liquid Nitrogen (LN2) Calibrations.....	11
4. Random Noise	12
Evaluating the Random Noise on the Black Body Temperature, ϵT_{BB}	13
Evaluating the Radiometric Resolution, $NE\Delta T$	13
Evaluating ϵT_{ND}	15
Error Covariance Matrix	20
Summary of all Random Noise.....	23
5. Systematic Errors (Bias)	24
Black Body Temperature.....	24
T_{ND} derived from Tip Curve Calibrations	24
Detector Non-Linearity.....	33
Temperature Dependence of T_{ND}	33
Summary of all Systematic Errors.....	35
6. Observed v Modelled Brightness Temperatures in Clear Air	36
Radiative Transfer Models of Clear Air Absorption	36
Procedure.....	37
Results for Software v2.14.....	38
Results for Software v2.20.....	39
Random Noise Budget for Comparison of Observed and Modelled T_b	41
7. Conclusions and Recommendations	43
Specific Recommendations for Radiometer Manufacturer	43
Specific Recommendations for Upper Air Technology Centre.....	43
8. References	44

1. Executive Summary

A microwave radiometer was procured from Radiometrics Corporation to evaluate its capabilities of providing profiles of temperature, humidity and cloud in the lower troposphere. This is part of the "Automation of Temperature and Humidity Profiles In The Lower Troposphere" Project [File Ref. M/O(OD)2U/8/5].

The radiometer has been operated at Camborne from 20 February 2002 to 18 March 2003. During this period the radiometer has proved to be very reliable, and needed only occasional intervention and calibration every few months by liquid nitrogen. The required interval is under review, but the procedure for these calibrations has now been agreed by Health & Safety.

During the first 11 months of the trial, the radiometer made one measurement every 14 minutes. The atmospheric variability can be significant over this period, and a software modification now allows the observation cycle to be improved to allow 1 measurement approximately every 2 minutes. Currently, the radiometer samples each channel sequentially, taking 40 s to integrate measurements from all 12 channels. We are still concerned that atmospheric changes during this period may degrade the retrievals in rapidly changing conditions. This will be addressed by a future firmware upgrade.

Radiometer noise is within specifications, which are adequate to retrieve some information on the structure of the lower troposphere. However, two of the channels are much noisier than the others. The cause of this should be investigated. Several modifications to the processing are suggested to further reduce the noise contribution from the calibration, especially noise that is correlated between different channels, as this will degrade the vertical resolution of the retrievals.

Substantial biases were found in the brightness temperatures in both the oxygen band channels and the water vapour channels with comparison with forward modelled brightness temperatures. These biases were found to impact the retrieved profiles as well. The biases in the oxygen channels have been reduced by a new release of the control software. The biases in the water vapour channels are found to be related to the total humidity, and are believed to be due to a bias in the forward model. This is under further investigation.

Development is underway of a variational method to assimilate data from the radiometer into Numerical Weather Prediction models. To optimise the use of these data, it is essential to understand the error characteristics of the radiometer, which are discussed in this report.

During the trial, a good working relationship has been established with the manufacturer, which has resulted in a number of improvements already. Further feedback is being supplied to enable the development of a radiometer optimised for operational use.

2. Introduction

A microwave radiometer was procured from Radiometrics Corporation to evaluate its capabilities of providing profiles of temperature, humidity and cloud in the lower troposphere. This is part of the “Automation of Temperature and Humidity Profiles In The Lower Troposphere” Project.

On 3 February 2003, after almost 1 year of operating at Camborne, new control software, v2.20 was installed on the radiometer, replacing v2.14. This introduced several improvements to the observation cycle, so data since then will be analysed separately in this report.

This report first describes the radiometer and the principles of its operation and calibration. We then go on to describe a series of tests that have been conducted to analyse its performance during the trial.

Section 4 presents the random noise budget. This determines how much impact the radiometer data can have on the NWP fields into which it will be assimilated. Section 5 describes the systematic errors that occur in the calibration of the instrument, and the uncertainties in them, which determine the accuracy of the radiometer data, and hence the profile retrieved using a neural network. The radiometer’s performance is also assessed by comparing the brightness temperatures with modelled data using radiosondes as ground truth (Section 6).

Finally, there is a summary of the conclusions and recommendations for future development needed to optimise the use of its data in NWP.

3. Description of Radiometer

The Radiometrics MP3000 is a microwave radiometer designed to retrieve temperature, humidity and cloud profiles in the lower troposphere. It is enclosed in a US style “mailbox”, mounted on a tripod, as shown in Figure 1. The system also include sensors for atmospheric pressure, temperature and humidity, a rain sensor, as well as an infrared radiometer (Heimann KT19.85) to measure the cloud base temperature. This views zenith through a small gold plated mirror on the top of the instrument enclosure.

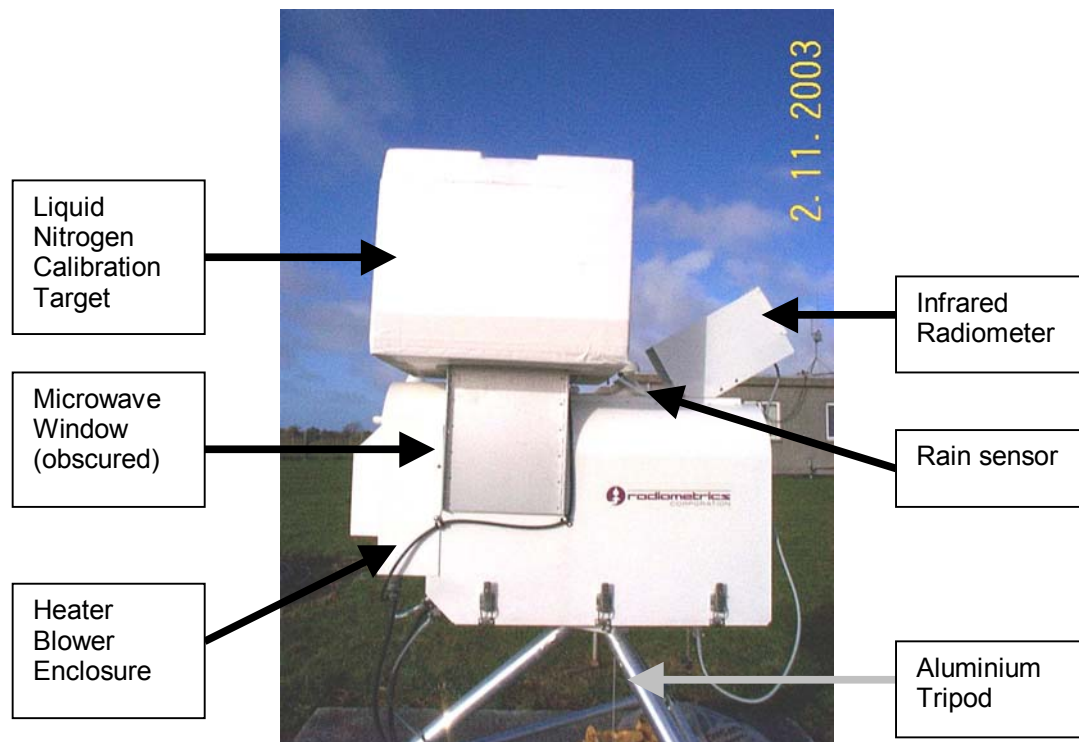


Figure 1 - Radiometrics MP3000 Microwave Radiometer, mounted on aluminium tripod with polystyrene calibration target filled with Liquid Nitrogen [Courtesy of Mike Exner]

The microwave radiometer nominally views in the zenith direction. Incoming radiation is transmitted through a proprietary microwave dielectric window onto a planar mirror and into a Gaussian Optics Antenna, comprising a dielectric lens, polarising grid (to couple both bands onto a common axis) and two corrugated feedhorns. These feed two independent receiver chains, which are mounted in thermally insulated enclosures. See Figure 2.

Microwave Window

The microwave dielectric window has a loss of approximately 0.01 dB at K band [Mike Exner, Radiometrics, personal communication]. Since the observations of the sky, LN2 target and tip curve data are all taken through the same window, the effect essentially "cancels out". Although the internal black body is not observed through the window, it does not matter since it is at approximately the same temperature as the window.

However, this is only true where the loss of the window is constant. This is not always the case when part of the window is wet, especially during tip curve calibrations [see Section 5]. It may also be possible for leakage from the local oscillator to be reflected from surface of the window (or any other quasi-optical component) and produce interference back at the mixer. If the optical path changed by more than a fraction of a wavelength (~ 1 mm), for example when scanning in elevation this can introduce standing waves, which bias these observations. There is no evidence that these are significant. But it should be tested in the laboratory by tracking a reflective plate in front of the antenna to check for variation in the radiometer's output.

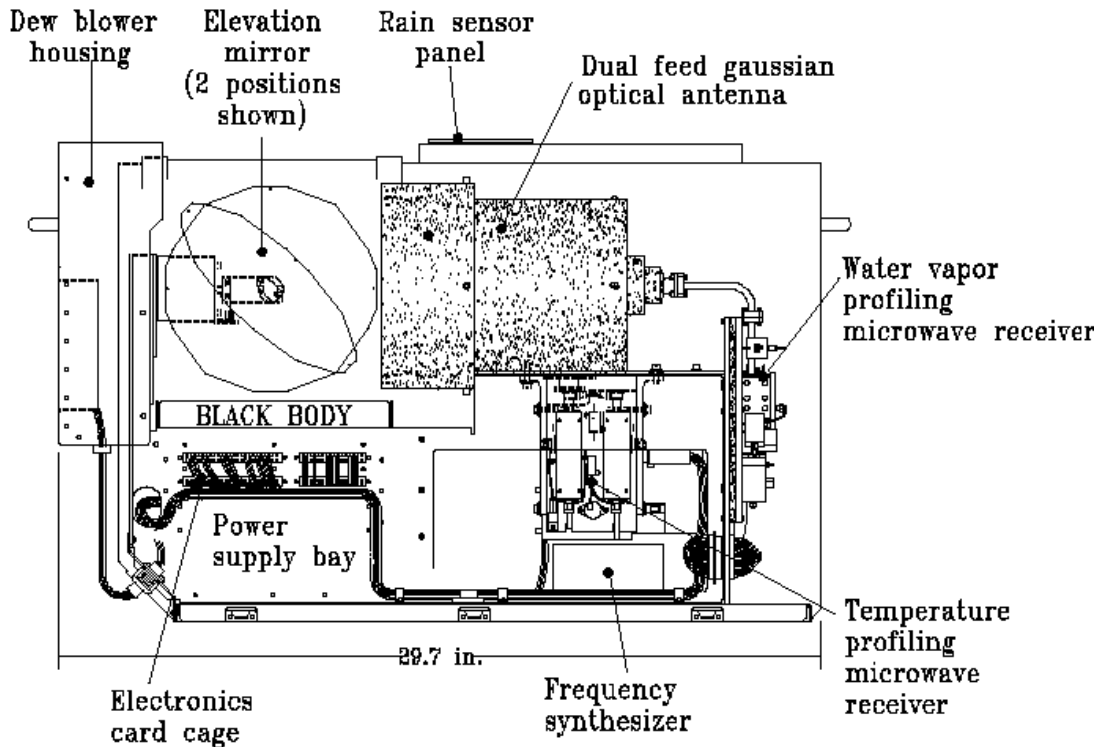


Figure 2 - Cross section of Microwave Radiometer MP3000 [Courtesy of Radiometrics]

Antenna

The antenna comprises all the quasi-optic components in the radiometer's front end: window, mirror, lens, diplexer and feedhorns. Together they define the antenna response function, which is approximately Gaussian, with the 3dB beamwidth ranging from 6.2° at 22.235 GHz to 2.4° at 58.8 GHz [Radiometrics, 2001]. The instrument's beamwidth is chosen as a trade-off between antenna size (and cost) and resolution. As most observations are done in the zenith direction, these relatively large beamwidths are acceptable. However, they become important when viewing at low elevation angles, for example during the tip curve calibrations. See Section 5.

These beamwidths were confirmed by using the Sun as a high brightness point source to map the antenna's response while the radiometer viewed due South with a fixed elevation for 2 hrs around noon in clear skies on 17 March 2003. A small sidelobe was found at the lowest frequencies of -17 dB, 12° from the beam centre. This is not a concern in itself, unless the Sun is present in this position. However, it is indicative of a low beam efficiency, which may bias the tip curve calibration.

The Microwave Receivers

The feedhorn in each receiver is followed by a switchable noise diode. This acts as a reference signal with high brightness temperature to allow the gain of the radiometer to be characterised when viewing the internal black body. A mixer then heterodynes the incoming radiation with a reference Local Oscillator signal from a frequency synthesiser to produce an Intermediate Frequency (IF) signal, ranging from 0 – 300 MHz. The IF signal is then amplified and filtered before being converted to an analogue signal by square law diode detectors, whose output voltage is proportional to their input power. Figure 3 shows a block diagram of the receivers.

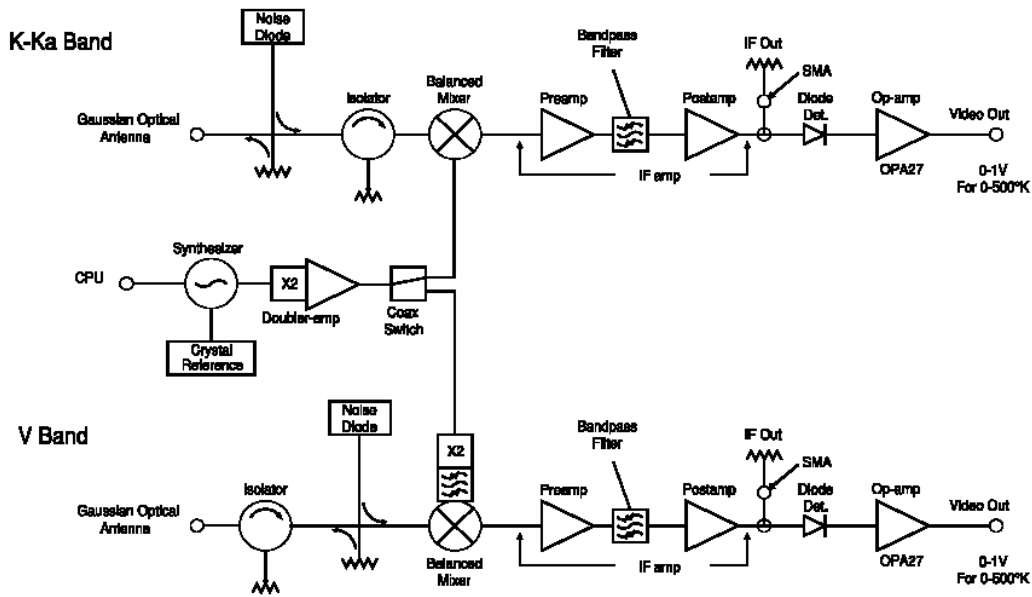


Figure 3 - Block Diagram of receivers in MP3000 [Courtesy of Radiometrics]

Channel Frequencies

It is nominally a 12-channel instrument, although in practice any combination of channels can be selected within the following bands: 22 – 30 GHz and 51 – 59 GHz. Each band is received and detected independently, although all channels use a common frequency synthesiser, which must be switched to observe each channel. In the current hardware configuration, it takes ~2 s to switch frequencies, although this may be reduced substantially in the future. This results in the observations not being coincident in all channels, and taking ~40 s to sample a set of 12 channels. Atmospheric variability during this period can introduce random noise on the observations, discussed in Section 4.

Radiometrics have suggested the sampling will be improved with future firmware upgrades to the existing hardware. This will allow much more rapid switching between channels so their integration periods could be multiplexed to reduce the effective time between observations in different channels to ~1 s. This will require a substantial overhaul of the control and processing software. It is anticipated that these changes will be offered to owners of existing radiometers during 2003.

The centre frequencies of the channels, given in Table 2, have remained unchanged during this trial. These values were derived as an optimal set by selecting those frequencies, which produced Eigenvalues with the maximum information content [Solheim *et al.*, 1996]. However, this analysis was based on radiative transfer models run using radiosonde data from Denver, Oklahoma City and West Palm Beach (FL), which may not be applicable to the British climate.

Each channel has dual sidebands, with 3dB bandwidths of 150 MHz, centred 115 MHz from the channel centre, which is defined by the 6-stage bandpass filter. So it detects radiation in the band $\pm(40 - 190)$ MHz each side of the centre frequency.

The stability of the frequency synthesiser is 20ppm, which is equivalent to <100 kHz at 60 GHz. This is not expected to contribute a significant uncertainty in the radiative transfer modelling.

Observation Cycle

Originally the radiometer was supplied with control software v2.14. This provided an default observation cycle of ~14 minutes, during which it would view the black body to measure the radiometer's gain and offset, attempt one tip curve and take one set of zenith brightness temperature measurements and retrieve a profile. If the rain sensor indicated rain, it would skip the tip curve, which reduced the observation cycle to ~7 minutes. A breakdown of the timing is given in Table 1.

Table 1 - Observation Cycle in minutes and seconds

	v2.14		v2.20 4_min.prc		v2.20 4_min.prc	
	Dry	Rainy	Normal		Around noon	
Black Body	03:39	03:39	01:00		01:00	
Tip Curve	06:15		00:40		00:40	
Zenith View	01:06	01:06	01:40		01:00	
Miscellaneous	03:06	03:06	00:40		00:40	
Total	14:06	07:51	04:00		04:00	

As a result of feedback from our trial, Radiometrics released a new version of the control software to improve the observation cycle, and reduce the radiometer biases.

Since 3 February 2003, the radiometer has been operated using v2.20 of the control software. This allows much greater control of the observation cycle. By default, it integrates each view for 0.5 s, and doesn't allocate so much time to pre-heating the noise diodes to ensure they are stable, as this was found to make no difference. This greatly speeds up the observing cycle. The impact of reducing the integration time is addressed in Section 4.

After some initial experiments, it was configured to observe in a 4-minute cycle: "4_min.prc". During this time, it views the black body, attempts a tip curve (if it's not raining) and takes 2 sets of zenith observations, producing a retrieval from each one. The timings used in this report are summarised in Table 1, but may be changed.

It is important to maximise the fraction of time the radiometer is observing the sky for many reasons. Ultimately, increasing the integration time improves the signal to noise ratio. Higher sampling rates may allow more realistic representation of small-scale structure in the atmosphere. This is important to understand these features and for real-time neural network retrievals. The observations should be representative of the part of the atmosphere that is to be assimilated into the NWP model. This may require several observations to be averaged prior to assimilation.

Calibration Methods and System Equations

Microwave radiometers need huge gains to be able to detect atmospheric signals. However, the amplifiers' gain is very sensitive to temperature. Fluctuations in temperature and voltages contribute random noise to the signal due to gain fluctuations, ΔG , according to Equation (4). To minimise these, the radiometer gain and offset must be measured frequently. This section addresses how this can be done. Section 5 will address how well this is done, and how frequently it will need to be done in future.

The offset of the radiometer is measured by regularly viewing the internal black body target. The gain is also calculated regularly by comparing the radiometer output while viewing the black body with the noise diode switched on and off. At present a simple linear transfer function is used to convert the detector voltages measured by the radiometer to brightness temperatures. This is given by the *system equation*:

$$T_b = T_{BB} - \frac{(V_{BB} - V_b)}{G} \quad (1)$$

where

$$G = \frac{(V_{BB+ND} - V_{BB})}{T_{ND}} \quad (2)$$

where T_b is the scene brightness (antenna) temperature,
 T_{BB} is the temperature of the black body target,
 V_{BB} , V_{BB+ND} and V_b are the voltage measured by the radiometer when viewing the black body, the black body plus the noise diode and the scene, respectively.
 G is the gain.
 T_{ND} is the brightness temperature of the noise diode.

In the future, a non-linear correction may be applied to the measurements. See Section 5.

The brightness temperature of the noise diode, T_{ND} is characterised by occasional views of a reference scene at a known brightness temperature, known as calibrations. In fact, T_{ND} includes a number of terms related to the loss of the receiver front end. This loss is dependent on the temperature of these components, so operationally a correction is applied based on the black body temperature and coefficients derived by Radiometrics during initial testing in an environmental chamber. The underlying assumption is that T_{ND} does not change significantly between calibrations. This assumption will be tested in Section 4.

Tip Curve Calibrations

The *tip curve* [Han & Westwater, 2000] is one method to derive an accurate reference scene temperature against which to calibrate a radiometer. This technique uses radiance measurements over a range of elevation angles calculated using an initial estimate of the calibration coefficients to derive an accurate estimate of the true radiance at zenith. This is then used to update the calibration coefficients. The underlying assumptions are that the atmosphere is horizontally stratified and optically thin, such that its opacity is a linear function of the slant path.

For a horizontally stratified, optically thin atmosphere, the radiative transfer equation can be simplified to the following expression for the down-welling brightness temperature, T_b , at zenith angle, θ :

$$T_b(\theta) = T_{MR} \cdot (1 - e^{-\tau \cdot \sec(\theta)}) + T_{CMB} \cdot e^{-\tau \cdot \sec(\theta)} \quad (3)$$

where T_{MR} is the mean radiative temperature of the atmosphere,
 T_{CMB} is the effective brightness temperature of the cosmic microwave background,
 τ is the opacity at zenith angle, θ .

The opacity over a range of zenith angles is calculated from measured brightness temperatures, using Equation (3), based on an initial calibration. For an optically thin, horizontally stratified atmosphere, the opacity is expected to increase linearly with slant path, $\sec(\theta)$.

In practice, every few minutes the radiometer takes measurements at 5 or 6 angles, symmetric around zenith. The measurements are then fitted against the theoretical function to derive an estimate of the true zenith brightness temperature. If the fit is deemed satisfactory, equations (1) and (2) are then inverted to adjust T_{ND} .

At present, tip curves are not attempted when rain is detected, as they are unlikely to pass. In Camborne's climate, this rejects 24.5 % of possible data. The quality control is based on the correlation coefficient between τ and $\sec\theta$, $r > 0.990$ for all channels in the water vapour band. 56.5 % of attempted tips from 22/2/02 – 3/2/03 were classed as successful.

A further quality control measure was introduced on 14 February 2003 to prevent the radiometer from attempting tip curves when there is a chance of the sun being near one of the fields of view. During the trial, the radiometer was aligned to tip in the North-South plane, so a simple time threshold of 11:24 – 13:30 is used. This corresponds to the range of times when the solar azimuth angle can fall within 12° of the tip curve views at Camborne. Although many tip curves fail during this period, there is a risk that marginal cases will bias the retrieved value of T_{ND} .

The values of T_{ND} for successful tips are logged in a file, and a weighted average of these is used to provide the 'current' value used in Equation (2). An exponential function is currently used, which reduces the weight on each subsequent calibration by 10 %, regardless of their distribution in time. This is a crude scheme that could be improved to greatly reduce the calibration noise.

The tip curve calibration process and an error budget are presented in Sections 4 and 5.

Liquid Nitrogen (LN2) Calibrations

The tip curve technique can only be applied to channels where the atmosphere is optically thin. So, another scheme is needed to calibrate T_{ND} for the oxygen-band channels. These channels are calibrated against an external black body at cryogenic temperatures.

The manufacturer supplied a calibration target, which comprises a box of expanded polystyrene foam, containing permeable microwave absorber. This is filled with liquid nitrogen and placed on top of the radiometer, so it views emissions from the absorber through the base of the polystyrene box, which has a low loss at microwave frequencies. This provides a black body at a low temperature that can be “accurately” calculated. The contrast between the radiometer measurements when viewing this and the internal black body near ambient temperatures is used to derive values of T_{ND} .

This procedure interrupts the regular observation cycle. Special software routines are provided to process these data. However, manual intervention is required to quality control and average the retrieved values of T_{ND} . The average value is then used until the next calibration. This procedure typically takes 1 – 2 hrs, after which the regular observation cycle is resumed.

Radiometrics recommend calibration every “several months”, or if the radiometer has been in storage, or after transporting the radiometer in case of rough handling [Radiometrics, 2001]. The error budget of these calibrations and the required frequency is analysed in Section 5.

After initial concerns were raised the calibration procedure has been revised, including lowering the radiometer to reduce the lifting involved. The revised procedure has now been agreed by Health & Safety.

4. Random Noise

Random noise is introduced in radiometric observations by thermal emission from every component to the receiver and antenna system (although it is usually dominated by 1 or 2 sources). This section estimates the magnitude of the random noise due to the instrument. Atmospheric fluctuations also introduce random noise, which will be considered later.

Random noise is arguably the most important single parameter of a radiometer, as it determines how useful its data can be to NWP. It is important to characterise the error covariance matrix, as this provides a weighting for the data relative to the background field when it is assimilated. It is also useful to minimise the random noise on the observations in order to better evaluate biases.

The radiometric resolution, $NE\Delta T$, (Noise Equivalent Differential Temperature) is defined as the minimum difference in scene brightness temperature that is resolvable at the radiometer's output. This is equivalent to the standard deviation of the brightness temperature measured by the radiometer while viewing a thermally stable scene. The radiometric resolution depends on the system noise temperature, T_{sys} , the pre-detection bandwidth, B , and the integration time, τ , and gain stability, according to Equation (4) [Ulaby *et al.*, 1981]:

$$NE\Delta T = T_{sys} \left[\frac{1}{B\tau} + \left(\frac{\Delta G}{G} \right)^2 \right]^{1/2} \quad (4)$$

where $\Delta G/G$ is the relative change in gain over the period between observations.

The system noise temperature, T_{sys} , is the sum of the receiver noise temperature, T_{rec} , and the antenna temperature, T_a :

$$T_{sys} = T_{rec} + T_a \quad (5)$$

T_a is closely related to the brightness temperature of the scene, T_b according to Equation (21). For convenience we shall use the term T_b interchangeably with T_a in the following.

However, $NE\Delta T$ is only due to the instrument itself. The final brightness temperatures will also suffer from noise introduced by the calibration process. This can be evaluated by differentiation of the system equations (1) and (2) to yield:

$$\varepsilon T_b^2 = \varepsilon T_{BB}^2 + 2 \cdot NE\Delta T^2 + \left[\frac{(T_{BB} - T_b)}{T_{ND}} \right]^2 \cdot (2 \cdot NE\Delta T^2 + \varepsilon T_{ND}^2) \quad (6)$$

where εT_{BB} is the uncertainty in the temperature of the black body, T_{BB} ,
 εT_{ND} is the uncertainty in brightness temperature attributed to the noise diode, T_{ND} ,
 εT_b is the uncertainty on the scene brightness temperature, T_b .

Note that εT_b derived from equation (6) contains $NE\Delta T$ terms multiplied by $\sqrt{2}$. This is due to the implementation of the system equation (1), which is applied independently to each observation cycle, differencing the views of the sky and the black body to account for the radiometer's offset.

The overall uncertainty on brightness temperature, εT_b could be reduced substantially (by as much as a factor of $\sqrt{2}$) if the derived offset could be averaged over a number of observation cycles. The gain is also calculated independently for each observing cycle. The noise on this term (3rd term in (6)) could also be reduced by averaging several gain measurements [McGrath & Hewison, 2001]. This is only true if the gain is measured (by viewing the BB and

BB+ND) more frequently than the typical timescales for gain variations. It is, however, difficult to test this using the existing format of the archived data sets, but it should be investigated. The optimal averaging periods for the gain and offset do not need to be the same and will depend on the design of the radiometer and its operating environment.

The following sections present a budget of each component of Equation (6). This allows us to identify which terms contribute most noise, and how they can be reduced. These results are then compared with statistically derived values in the form of the *Error Covariances*.

Evaluating the Random Noise on the Black Body Temperature, ϵT_{BB}

There are 2 AD592C temperature sensors mounted in the internal black body target. The standard deviation of the difference between the 2 temperature sensors is 0.068 K. This implies the standard uncertainty on the mean is 0.048 K. This may be due to thermal gradients or noise in the temperature sensors or their circuitry.

The mean difference is (1.7 ± 0.4) mK, and is independent of ambient temperature, rate of change of temperature, and contrast between black body and ambient temperatures. There is only a weak correlation between the rate of change of blackbody temperature and the rate of change of ambient temperature. (Slope= 0.45 ± 0.01 K/K). This shows that it is quite well isolated from environmental changes. The autocorrelation between these rates of change suggests a time constant of ~ 90 minutes for the black body target temperature.

The r.m.s. rate of change of blackbody target temperature over 1 year at Camborne is 1.61 K/hr. The typical period between the measuring the temperature and viewing the black body is 1 minute. This produces an uncertainty of 0.027 K in the temperature of the black body target. This is a significant fraction of the radiometric resolution of the instrument.

Overall, the random component of the uncertainty on the black body target temperature is the sum of the noise on the sensors (0.048 K) and the thermal stability (0.027 K in normal operation). Thus, the random component of the uncertainty is $\epsilon T_{BB} = 0.055$ K in normal operation (and slightly lower in stable conditions). This has a small impact in the calculation of $NE\Delta T$ using Equation (6).

An AR(3) Auto-regression model [Wilks, 1995] has been fitted to the measured time series of the black body temperature, T_{BB} . This model estimates the white noise variance as 8 mK for v2.20, but 68 mK for v2.14. However the actual noise will be less than this, in proportion to the difference in timing between the physical and radiative measurements of the black body target, relative to the observation period.

Evaluating the Radiometric Resolution, $NE\Delta T$

The radiometric resolution of the instrument is relatively straightforward to calculate from the standard deviation of the brightness temperatures measured while viewing a stable scene. A special observing cycle is available that allows the radiometer to view its black body twice in rapid succession – firstly to derive the calibration, then immediately afterwards to measure its brightness temperature. The average brightness temperature should equal the temperature of the black body, and its variance is a direct measure of ϵT_b with $T_b = T_{BB}$. In this case, Equation (6) reduces to:

$$NE\Delta T^2 = \frac{\epsilon T_b (T_{BB})^2 - \epsilon T_{BB}^2}{2} \quad (7)$$

This was originally evaluated under software v2.14 on 22 November 2002 during a period when the ambient temperature changed slowly, to minimise any thermal gradients in the target. The resulting time series of brightness temperatures are shown in Figure 4. Notice that some channels produce brightness temperatures systematically higher than T_{BB} !

This result was conveyed to the manufacturer, and was part of the motivation for upgrading to v2.20 of the control software. The same test was repeated immediately after installing the

new software on 3 February 2003. The brightness temperatures are shown over a similar period in the righthand panel of Figure 4. Note that the brightness temperatures are now sampled much more rapidly (1/82.4 s) than before (~1/300 s). They are also now distributed normally about T_{BB} , i.e. The bias has been removed by the software upgrade. However, the cause of the bias remains a mystery.

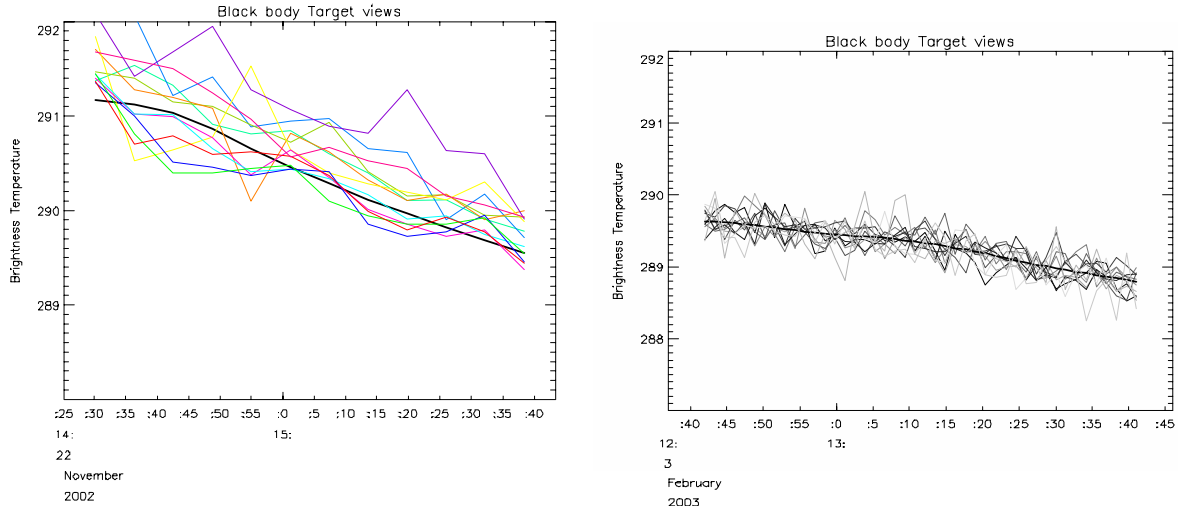


Figure 4 - Time series of Brightness Temperatures measured viewing Black Body. Thick Black line indicates physical temperature of Black Body. Different colours/shades of grey indicate different channels. Left panel shows bias with Software v2.14. Right panel is Software v2.20. Both ~1hr.

Table 2 shows the mean bias measured while viewing the ambient black body target for both versions of the control software. Values that are statistically significant ($>2\sigma$) are highlighted in **bold**. The bias in the high frequency channels is reduced to insignificant levels in v2.20.

Table 2 - Radiometric Resolution and Bias measured viewing ambient Black Body

Software	v2.14		v2.20	
Integration time (s)	1.0		0.5	
Frequency (GHz)	Bias (K)	$NE\Delta T$ (K)	Bias (K)	$NE\Delta T$ (K)
22.235	-0.06	0.11	-0.04	0.13
23.035	-0.13	0.10	-0.04	0.10
23.835	-0.12	0.10	0.03	0.09
26.235	-0.00	0.10	0.09	0.10
30.000	-0.03	0.09	-0.03	0.11
51.250	0.20	0.13	0.06	0.12
52.280	0.21	0.10	0.07	0.12
53.850	0.30	0.08	-0.02	0.10
54.940	0.25	0.08	-0.06	0.09
56.660	0.50	0.24	0.02	0.20
57.290	0.74	0.19	-0.07	0.18
58.800	0.39	0.09	-0.02	0.14

The calculated values of the radiometric resolution, $NE\Delta T$, are also given in Table 2. This shows the mean bias measured while viewing the ambient black body target for both versions of the control software. Statistically significant ($>2\sigma$) values are highlighted in **bold**. Although the integration time has been halved with the introduction of the new software, the $NE\Delta T$ has not increased by the factor of $\sqrt{2}$ expected. This is due to improvements in gain stability, $\Delta G/G$ in Equation (4) brought about by a reduction in the observation cycle.

The channels at 56.66 GHz and 57.29 GHz are consistently noisier than the other channels, even after the software change. These are the same channels that showed the largest bias under v2.14. This suggests there is a instrumental cause, such as interference from another component within the radiometer or without. The manufacturer should investigate this, as it is restricting the quality of the retrieved temperature profiles at the lower levels.

Evaluating ϵT_{ND}

The terms evaluated so far allow us to evaluate the random noise on measured brightness temperatures close to ambient, using Equation (6). Lower brightness temperatures, usually found in water vapour and low frequency oxygen channels, include a component attributed to the noise diode, ϵT_{ND} . As T_{ND} is evaluated by external calibration using tip curve or liquid nitrogen for the water vapour and oxygen channels respectively, the random noise introduced by these processes are analysed here.

Tip Curve – Radiometer Noise

Radiometer noise is present on all measurements that are used in the tip curve. This introduces a random uncertainty in the retrieved zenith brightness temperature, which is used as the reference point for the calibration. It is not expected to introduce any net bias. The noise is approximately the same for all the views of the tip curve.

Each observation in a tip curve is calculated using the same values of G , T_{ND} and T_{bb} , in Equation (1). If n observations are used to fit the tip curve, this effectively reduces the component of random noise due to the radiometric resolution, $NE\Delta T$, in Equation (6) by a factor of $1/\sqrt{n}$. However, other components of random noise due to the calibration remain the same. The resulting uncertainty is then propagated through to the retrieved zenith brightness temperature. Table 5 shows this term is small (≤ 0.15 K).

If the calibration for each point on the tip curve were derived independently, this term would become insignificantly small (at the expense of increasing the time taken to tip).

Tip Curve—Atmospheric Variability

Fluctuations in humidity associated with meteorological changes introduce a random error in the zenith brightness temperature retrieved by the calibration. They were also analysed by Han & Westwater [2000], but for a completely different climate. They used humidity measurements from a co-located Raman LIDAR to estimate r.m.s. calibration errors of 0.83 – 0.25 K for 23.8 – 31.4 GHz radiometers operating in the Southern Great Plains, USA.

The standard deviations of the difference between views on opposite sides of the tip curve are given in Table 3. These include radiometer noise, which must be subtracted to produce an estimate of the random variability of the atmosphere during each successful tip curve. Because each pair of observations made with v2.14 of the control software are calculated using the same values of G , T_{ND} and T_{bb} , in Equation (1), the uncertainty on the difference is $\sqrt{2}NE\Delta T$. The residual uncertainty is then propagated through to the retrieved zenith brightness temperature. The results using software v2.14 are shown in Table 3.

Table 3 - Noise on Zenith Brightness Temperature from Tip Curve Calibration due to Atmospheric Variability for Software v2.14 20/2/02 – 3/2/03

Frequency (GHz)	$NE\Delta T$ (K)	Variance of Tip Curve Brightness Temperatures (K)			Atmospheric Variability (Radiometer noise removed) (K)			Noise on Fitted Zenith T_b (K)
		$\pm 60^\circ$	$\pm 45^\circ$	$\pm 0^\circ$	$\pm 60^\circ$	$\pm 45^\circ$	$\pm 0^\circ$	
22.235	0.11	1.35	0.78	0.32	0.95	0.54	0.20	0.25
23.035	0.10	1.30	0.76	0.32	0.91	0.53	0.20	0.25
23.835	0.10	1.13	0.68	0.32	0.79	0.47	0.20	0.23
26.235	0.10	0.91	0.61	0.34	0.63	0.42	0.22	0.21
30.000	0.09	0.92	0.66	0.40	0.64	0.46	0.27	0.24

Software v2.20 changed the radiometric resolution, $NE\Delta T$, and has been modified to observe the same range of angles on the tip curve as v2.14. Since this change, conditions have been favourable to produce tip curves with lower atmospheric variability, reducing the noise on the fitted zenith T_b to ~ 0.15 K. Although the basic timing of the tip curve has been tightened up, these results are not believed to be generally the case, so values from Table 3 are expected to be more representative of the performance of the tip curves during a full year.

Tip Curve – Variability of Mean Radiative Temperature

The horizontal variability of the atmosphere has been accounted for above. The temporal variability also introduces random noise on the tip curve calibration on long time scales. At present, constant values of mean radiative temperature, T_{MR} , are assigned to each channel. After temperature correction, T_{MR} has been found to vary with an r.m.s. of 2.9 K at Camborne. This introduces an uncertainty to T_{ND} derived from the tip curve proportional to opacity. As summarised in Table 5, it is a significant term for the lowest frequency water vapour channels, and dominates the error budget when attempting to apply the tip curve to oxygen channels.

It may be possible to reduce the noise introduced by this term by a factor of ~ 2 , by estimating the mean radiative temperature using the profiles retrieved by the radiometer. This should be investigated by the manufacturer.

It should also be noted that this term will not be reduced much by the exponential averaging used for the tip curves, as it is likely to be correlated over periods of ~ 1 day.

True T_{ND} variability

In addition to the noise introduced by the calibration, genuine variability of the noise diode also introduces random noise to the brightness temperatures. Although it is attributed to the noise diode, in fact, it includes contributions from all the front-end components of the radiometer. In general, it comprises two components – a random part, and a temperature dependent part, which is dealt with in Section 5.

This term may be evaluated by analysing the variability of T_{ND} between calibrations separated by a range of intervals. However, in practice calibrations are normally dominated by the other terms, described in the preceding sections. So, it is only possible to isolate the true receiver variability by applying filters to a time series of calibrations to minimise each of these terms.

The r.m.s. difference is calculated between T_{ND} values derived from pairs of calibrations. This is calculated for all possible pairs of calibrations and the results are then averaged over bins of logarithmically increasing periods. The results are then divided by $\sqrt{2}$ to estimate the [Allan Deviation](#), $\sigma_y(\tau)$ which increases with the interval between calibrations, τ , as:

$$\sigma_y(\tau) = \sigma_{y0} \cdot \tau^\beta \quad (8)$$

where σ_{y0} is the Allan Deviation for an arbitrary period of $\tau=1$ s, and β is a constant. For a non-stationary process that can be represented as a random walk, $\beta=0.5$. Generally, $0 < \beta < 1$.

This follows the intuitive result that the longer the interval since the last calibration, the more uncertainty is introduced by extrapolating it.

Filters were applied successively to archived series of tip curves taken with the same instrument configuration, after temperature compensation of T_{ND} . $\sigma_y(\tau)$ was calculated after each filter. It was found that the results tended to converge to a minimum value after rejecting calibrations where the infrared brightness temperature, $T_{IR} > 240$ K, which implies only calibrations with no low cloud are used. The effect of changing this threshold and introducing further filters, based on the rate of change of brightness temperature were investigated, but found not to produce further improvements in $\sigma_y(\tau)$ and reduced the available dataset.

The results are shown in Figure 5 before and after applying the $T_{IR} < 240$ K filter to tip curve calibrations taken with software v2.20 at Camborne between 14/2/03 – 18/3/03.

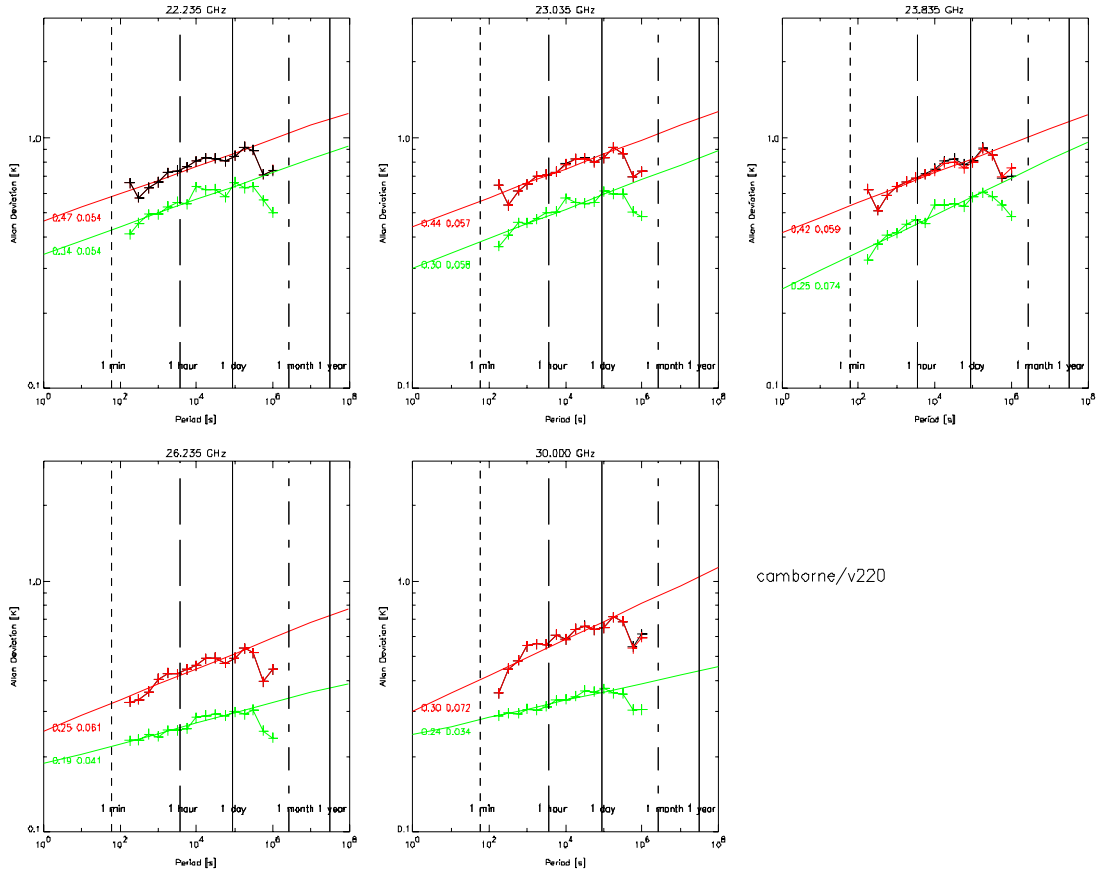


Figure 5 – Allan Deviation of T_{ND} for Camborne v2.20 14/2/03 – 18/3/03

Red = Calculated from all calibration data

Green = Only using data where $T_{ir} < 240$ K (no low cloud)

The results show large improvements in the stability of the calibrations may be achieved by rejecting situations with low cloud. There is already some filtering applied in the original quality control of the tip curves, which requires the correlation coefficient, $r > 0.99$. However, the additional filtering also increases the average time between calibrations, which cancels out some of the benefits. This is assumed to be an estimate of the upper bound of the true receiver variability in T_{ND} and should be included in the total error budgets.

When applying the calibrations, T_{ND} is averaged using an exponential weighting of the form:

$$\langle T_{ND} \rangle_i = (1-f) \cdot \langle T_{ND} \rangle_{i-1} + f \cdot T_{ND_i} \tag{9}$$

where i indicates the current timestep, and f is the weighting factor, currently $f = 0.1$.

The effect of this is to reduce the random noise. The standard deviation decreases by a factor of $\sqrt{f/2}$. However, the exponential averaging also increases the lag between the average time of the calibration dataset and the current observation. This average lag, $\langle \tau \rangle$ is calculated as a logarithmic average of the time difference between each calibration and the current observation. With no additional filtering, this lag was found to be $\langle \tau \rangle = 8$ hrs with a 14 minute observation cycle at Camborne. When the observation cycle was reduced to 4 minutes, the lag reduced to $\langle \tau \rangle = 4$ hrs. When the cloud filter is introduced, this increases the lag period by a factor of ~ 4 at Camborne, which results in increased variability, and cancels out some of the benefit of reducing the Allan Deviation, as shown in Table 4.

The increased sampling rate with software v2.20 did not result in a net reduction in the noise on the tip curves substantially, even though it reduced the average lag period by a factor of 2.

**Table 4 - Allan Deviation of T_{ND} for Camborne v2.14 and v2.20
– instantaneous and at average lag period of exponential average
– before and after filtering out low cloud ($T_{ir} < 240$ K)**

All tips $T_{ir} < 320$ K			v2.14		v2.20		hrs
			Latest Tip only	Exp Average	Latest Tip only	Exp Average	
Frequency [GHz]	σ_{τ} [K]	β	$\sigma_{\tau}(\tau)$ [K]	$\sigma_{\tau}(\tau)$ [K]	$\sigma_{\tau}(\tau)$ [K]	$\sigma_{\tau}(\tau)$ [K]	
22.235	0.47	0.054	0.75	0.18	0.72	0.18	
23.035	0.44	0.057	0.72	0.18	0.69	0.17	
23.835	0.42	0.059	0.70	0.17	0.67	0.17	
26.235	0.25	0.061	0.42	0.10	0.40	0.10	
30.000	0.30	0.022	0.36	0.08	0.36	0.08	
No Low Cloud $T_{ir} < 240$ K			Latest Tip only	Exp Average	Latest Tip only	Exp Average	hrs
			8.8	30.0	5.9	15.7	
Frequency [GHz]	σ_{τ} [K]	β	$\sigma_{\tau}(\tau)$ [K]	$\sigma_{\tau}(\tau)$ [K]	$\sigma_{\tau}(\tau)$ [K]	$\sigma_{\tau}(\tau)$ [K]	
22.235	0.34	0.054	0.59	0.14	0.58	0.14	
23.035	0.30	0.058	0.55	0.13	0.53	0.13	
23.835	0.25	0.074	0.54	0.13	0.52	0.13	
26.235	0.19	0.041	0.29	0.07	0.29	0.07	
30.000	0.24	0.034	0.34	0.08	0.34	0.08	

There is a remaining concern that only selecting tip curves when the atmosphere is well stratified, horizontally homogenous and cloud free may produce biased calibrations when applied to other conditions. For example, if the microwave window is wet. However, on the few occasions that the original tip curve passed the quality control in these conditions, the exponential average would not be representative.

In theory the same technique could be applied to LN2 calibrations. However, there was too much difference between calibrations due to changes in the target design. Also, the typical duration (~1 hr) and separation (~2 months) leaves critical time scales under represented in the resulting Allan Deviation. For these reasons, the stability of the oxygen channels is assumed to be equal to the average of the water vapour channels.

Total Noise Budget for Tip Curve Calibrations

Table 5 summarises the above contributions to the random error budget of the tip curve calibration. Although these mechanism affect T_{ND} , they have been translated to the equivalent uncertainty on typical zenith brightness temperatures for ease of comparison. It is clear that atmospheric variability and uncertainty in estimating the mean radiative temperature are the dominant sources of random noise. The later renders the tip curve technique useless for the oxygen channels, although there is scope for improving this as described above.

Table 5 - Summary of Random Noise on Tip Curve Calibrations v2.14

Frequency (GHz)	Tb Nominal (K)	Radio meter Noise (K)	Atmos. Noise (K)	Tmr Noise (K)	Tnd Drift (K)	Total Noise (K)
22.235	27.5	0.08	0.27	0.26	0.12	0.40
23.035	27.0	0.08	0.26	0.25	0.11	0.39
23.835	24.0	0.07	0.24	0.22	0.11	0.35
26.235	17.1	0.08	0.22	0.15	0.10	0.29
30.000	15.0	0.07	0.25	0.12	0.11	0.31
51.250	105.5	0.10	0.19	1.09	0.08	1.11
52.280	148.9	0.08	0.15	1.55	0.06	1.56
53.850	248.6	0.06	0.07	2.62	0.02	2.62
54.940	278.7	0.15	0.06	2.81	0.01	2.82
56.660	283.4	0.03	0.10	2.88	0.01	2.89
57.290	283.8	0.00	0.08	2.90	0.01	2.90
58.800	284.1	0.00	0.05	2.90	0.01	2.90

Total Noise Budget for Liquid Nitrogen Calibrations

A liquid nitrogen calibration typically lasts ~1 hr. During this time, multiple measurements ($n \sim 20$) are made and averaged together to estimate T_{ND} . This reduces the impact of radiometer noise to a negligible level. There is a small residual variation in the average, which is attributed to fluctuations in the boiling point of nitrogen.

However, the random noise on T_{ND} due to the LN2 calibration is dominated by drift in the radiometer system. As was described in the preceding section, it is very difficult to quantify this from LN2 calibrations. So here, we assume the channels in the oxygen band suffer from the same average drift as the water vapour channels, relative to T_{ND} . This is summarised in Table 6, expressed in terms of uncertainty on typical zenith brightness temperatures. This shows the total random noise budget for the LN2 calibration closely matches the variance of T_{ND} observed from successive calibrations.

Table 6 - Summary of Random Noise on LN2 Calibrations v2.14

Frequency (GHz)	Tb Nominal (K)	LN2 Noise (K)	Tnd Drift (K)	Total Noise (K)	TND Stats (K)
22.235	27.5	0.07	0.63	0.63	0.63
23.035	27.0	0.06	0.60	0.60	0.81
23.835	24.0	0.06	0.64	0.64	0.86
26.235	17.1	0.10	0.52	0.53	0.72
30.000	15.0	0.09	0.53	0.54	0.90
51.250	105.5	0.07	0.42	0.42	0.67
52.280	148.9	0.04	0.32	0.32	0.48
53.850	248.6	0.01	0.11	0.11	0.16
54.940	278.7	0.00	0.04	0.04	0.05
56.660	283.4	0.01	0.03	0.03	0.12
57.290	283.8	0.01	0.03	0.03	0.07
58.800	284.1	0.00	0.03	0.03	0.07

Error Covariance Matrix

The *Observation Error Covariance Matrix* is an important characteristic of the radiometer, which is needed in variational assimilation of its data. It can be estimated from time series of calibration data, by re-writing Equation (6) in matrix notation:

$$S_{T_b} = S_{T_{bb}} + 2 \cdot S_{NEAE} + \left[\frac{(T_{BB} - T_b)}{T_{ND}} \right]^T \left[\frac{(T_{BB} - T_b)}{T_{ND}} \right] \cdot (2 \cdot S_{NEAE} + S_{T_{ND}}) \tag{10}$$

where S_{NEAT} is the error covariance matrix of the uncalibrated radiometer noise, $NEAT$,
 S_{T_b} is the error covariance matrix of the brightness temperature vector, T_b
 $S_{T_{bb}}$ is the error covariance matrix of the black body target temperature, T_{bb}
 $S_{T_{ND}}$ is the error covariance matrix of the black body target temperature, T_{ND}

The variance-covariance matrix, S is a symmetric ($K \times K$) matrix, whose diagonal elements are the sample variances of K variables, and whose other elements are the covariances among the variables [Wilks, 1995]. In variational assimilation, S is known as the *Error Covariance Matrix* [Eyre, 1991]. It is defined by:

$$S = (n-1)^{-1} Y'^T Y' \tag{11}$$

where Y' is the ($n \times K$) matrix of brightness temperature anomalies from the mean of n observations in K channels.

Evaluating S_{NEAT}

S_{NEAT} can also be estimated from the same measurements of the black body used to calculate $NEAT$ in Table 2. Like $NEAT$, this does not include random noise introduced by the calibration when viewing scene brightness temperatures different to ambient. Table 7 and Table 8 show the resulting error covariance using software v2.14 and v2.20 respectively. While the earlier results had substantial off diagonal terms in the lowest and highest frequency channels, these become very small after the software upgrade.

Table 7 - S_{NEAT} evaluated viewing Black Body with Software v2.14 (K^2)

22.235	23.035	23.835	26.235	30.000	51.250	52.280	53.850	54.940	56.660	57.290	58.800GHz
0.011	0.006	0.005	0.004	0.004	0.004	0.001	0.001	0.001	-0.001	0.002	0.000
0.006	0.010	0.006	0.003	0.003	0.004	0.002	0.001	0.000	-0.000	0.002	0.000
0.005	0.006	0.009	0.004	0.004	0.004	0.001	0.000	0.001	0.001	0.001	0.001
0.004	0.003	0.004	0.011	0.002	0.003	0.003	0.000	0.001	0.003	0.005	0.000
0.004	0.003	0.004	0.002	0.009	0.003	-0.000	-0.001	0.000	0.002	0.000	0.000
0.004	0.004	0.004	0.003	0.003	0.018	0.002	0.002	0.001	-0.001	0.003	0.001
0.001	0.002	0.001	0.003	-0.000	0.002	0.011	0.001	0.001	0.001	0.003	0.000
0.001	0.001	0.000	0.000	-0.001	0.002	0.001	0.007	0.001	-0.002	0.001	0.001
0.001	0.000	0.001	0.001	0.000	0.001	0.001	0.001	0.007	-0.002	-0.001	0.001
-0.001	-0.000	0.001	0.003	0.002	-0.001	0.001	-0.002	-0.002	0.058	0.013	-0.005
0.002	0.002	0.001	0.005	0.000	0.003	0.003	0.001	-0.001	0.013	0.036	0.003
0.000	0.000	0.001	0.000	0.000	0.001	0.000	0.001	0.001	-0.005	0.003	0.009

Table 8 - S_{NEAT} evaluated viewing Black Body with Software v2.20 (K^2)

0.017	0.000	0.000	-0.002	0.002	-0.004	-0.001	0.002	0.003	0.002	-0.003	0.006
0.000	0.010	0.001	-0.003	-0.001	0.000	-0.002	-0.000	0.000	0.001	0.003	-0.002
0.000	0.001	0.008	-0.001	-0.002	-0.001	0.002	0.002	-0.000	-0.001	-0.001	-0.000
-0.002	-0.003	-0.001	0.009	-0.002	-0.001	0.001	0.001	-0.000	-0.004	-0.000	-0.002
0.002	-0.001	-0.002	-0.002	0.011	0.001	-0.000	-0.000	-0.001	0.004	-0.001	-0.001
-0.004	0.000	-0.001	-0.001	0.001	0.014	-0.002	-0.000	-0.002	-0.003	-0.000	-0.001
-0.001	-0.002	0.002	0.001	-0.000	-0.002	0.014	-0.001	-0.000	0.001	-0.004	-0.001
0.002	-0.000	0.002	0.001	-0.002	-0.000	-0.001	0.011	0.002	0.001	0.000	0.001
0.003	0.000	-0.000	-0.000	-0.000	-0.001	-0.002	-0.000	0.002	0.008	-0.001	0.002
0.002	0.001	-0.001	-0.004	0.004	-0.003	0.001	0.001	-0.001	0.039	0.005	0.000
-0.003	0.003	-0.001	-0.000	-0.001	-0.000	-0.004	0.000	0.002	0.005	0.031	-0.000
0.006	-0.002	-0.000	-0.002	-0.001	-0.001	-0.001	0.001	0.001	0.000	-0.000	0.018

Evaluating S_{TND} for Water Vapour Channels

S_{TND} can be estimated from time series of tip curve calibrations. The exponential averages, $\langle T_{ND} \rangle$ are analysed over samples within a window representing the timescale used in the calibration, $\langle \tau \rangle$. This has been evaluated as $\langle \tau \rangle = 4$ hrs [from Table 4]. This calculation was repeated for all such samples within the period 14/2/03 – 18/3/03, using software v2.20 with a 4 minute observation cycle, and tip angles $\pm 30^\circ$, $\pm 45^\circ$ and 90° . The average value of S_{TND} is shown in Table 9.

Table 9 - S_{TND} evaluated from tip curves 14/2/03 – 18/3/03 with Software v2.20 (K^2)

22.235	23.035	23.835	26.235	30.000	GHz
0.047	0.044	0.042	0.021	0.025	
0.044	0.045	0.042	0.022	0.026	
0.042	0.042	0.044	0.022	0.027	
0.021	0.022	0.022	0.013	0.016	
0.025	0.026	0.027	0.016	0.022	

The covariance matrix, S_{TND} , shown in Table 9 has strong off diagonal terms, which will degrade the vertical resolution of humidity profiles retrieved with this configuration.

S_{TND} may be reduced by 16 – 50 % by rejecting tip curve calibrations that may be influenced by low cloud, even though this increases the timescale, $\langle \tau \rangle$ over which calibrations must be averaged to ~ 8 hrs. This is simple to implement using a simple threshold on the infrared brightness temperature, $T_{IR} < 240$ K.

Evaluating S_{TND} for Oxygen Channels

It is not so straightforward to estimate S_{TND} for the oxygen channels. Although liquid nitrogen calibrations can be analysed, a large variability was found between calibrations, due to changes in the target design and procedures during the trial. It is, however, possible to estimate S_{TND} from individual observations within a single LN2 calibration.

Firstly, the time series of T_{ND} is converted to T_b using a nominal calibration. The covariance of this is calculated, $S_{Tb(LN2)}$, which includes components due to scene variability, radiometer noise and T_{ND} drift. As both $S_{Tb(LN2)}$ and S_{NEAT} were estimated on timescales of ~ 1 hr, the radiometer noise can be removed by inverting Equation (10) to estimate S_{TND} as shown in Table 10.

Table 10 - S_{TND} evaluated from LN2 calibration 11/2/03 with Software v2.20 (K^2)

22.235	23.035	23.835	26.235	30.000	51.250	52.280	53.850	54.940	56.660	57.290	58.800	GHz
-0.031	0.036	-0.005	0.015	0.001	0.044	0.034	-0.014	-0.011	-0.010	-0.017	-0.047	
0.036	0.029	0.027	0.036	0.026	-0.012	0.054	0.009	0.016	0.007	-0.037	0.010	
-0.005	0.027	0.013	0.017	0.006	0.018	-0.003	0.006	-0.004	-0.005	-0.026	0.008	
0.015	0.036	0.017	0.021	0.023	0.015	0.008	-0.009	0.007	0.013	-0.011	0.010	
0.001	0.026	0.006	0.023	0.027	0.012	0.021	0.005	0.006	0.016	0.025	0.029	
0.044	-0.012	0.018	0.015	0.012	0.049	0.036	0.017	-0.002	0.022	0.000	-0.008	
0.034	0.054	-0.003	0.008	0.021	0.036	0.065	0.028	0.023	0.068	0.041	-0.002	
-0.014	0.009	0.006	-0.009	0.005	0.017	0.028	0.009	0.011	0.009	-0.028	0.029	
-0.011	0.016	-0.004	0.007	0.006	-0.002	0.023	0.011	0.059	0.024	-0.010	0.018	
-0.010	0.007	-0.005	0.013	0.016	0.022	0.068	0.009	0.024	-0.015	0.032	0.022	
-0.017	-0.037	-0.026	-0.011	0.025	0.000	0.041	-0.028	-0.010	0.032	0.030	0.011	
-0.047	0.010	0.008	0.010	0.029	-0.008	-0.002	0.029	0.018	0.022	0.011	0.019	

Note that this calculation is very noisy. Even some of the diagonal terms of S_{TND} are negative! This is because the calculation involves differencing noisy covariances. However, on average, the diagonal and off-diagonal terms are significantly non-zero: $0.023 \pm 0.008 K^2$ and $0.010 \pm 0.002 K^2$ respectively. As a very crude approximation, S_{TND} could be approximated as a diagonal matrix with these terms evenly distributed.

S_{TND} also needs to be scaled from the timescale over which the samples were taken ($\tau_1 \sim 1$ hr) to a timescale typical of the interval between LN2 calibrations, $\tau_2 \sim 1$ month. This can be done by multiplying the resulting covariance matrix by the factor $(\tau_2/\tau_1)^\beta \sim 1.4$, where $\beta = 0.051$ is the average of the values calculated for the K-band channels, given in Table 4.

Finally, S_{TND} from the tip curve and liquid nitrogen calibrations can be combined, by assuming the two methods are mutually independent. This results in a covariance matrix shown in Table 11.

Table 11 - S_{TND} combined from tip curves and LN2 calibrations with Software v2.20 (K^2)

22.235	23.035	23.835	26.235	30.000	51.250	52.280	53.850	54.940	56.660	57.290	58.800GHz
0.047	0.044	0.042	0.021	0.025	0.000	0.000	0.000	0.000	0.000	0.000	0.000
0.044	0.045	0.042	0.022	0.026	0.000	0.000	0.000	0.000	0.000	0.000	0.000
0.042	0.042	0.044	0.022	0.027	0.000	0.000	0.000	0.000	0.000	0.000	0.000
0.021	0.022	0.022	0.013	0.016	0.000	0.000	0.000	0.000	0.000	0.000	0.000
0.025	0.026	0.027	0.016	0.022	0.000	0.000	0.000	0.000	0.000	0.000	0.000
0.000	0.000	0.000	0.000	0.000	0.032	0.014	0.014	0.014	0.014	0.014	0.014
0.000	0.000	0.000	0.000	0.000	0.014	0.032	0.014	0.014	0.014	0.014	0.014
0.000	0.000	0.000	0.000	0.000	0.014	0.014	0.032	0.014	0.014	0.014	0.014
0.000	0.000	0.000	0.000	0.000	0.014	0.014	0.014	0.032	0.014	0.014	0.014
0.000	0.000	0.000	0.000	0.000	0.014	0.014	0.014	0.014	0.032	0.014	0.014
0.000	0.000	0.000	0.000	0.000	0.014	0.014	0.014	0.014	0.014	0.032	0.014
0.000	0.000	0.000	0.000	0.000	0.014	0.014	0.014	0.014	0.014	0.014	0.032

Evaluating Overall Observation Error Covariance Matrix, S_{Tb}

S_{TND} is then combined with S_{NEAT} using Equation (10), to estimate the overall *Observation Error Covariance Matrix* for typical scene brightness temperatures, S_{Tb} given in Table 12.

Table 12 - Overall Observation Error Covariance Matrix, S_{Tb} for typical scene brightness temperatures, including calibration noise combined from tip curves and LN2 calibrations with Software v2.20 (K^2)

22.235	23.035	23.835	26.235	30.000	51.250	52.280	53.850	54.940	56.660	57.290	58.800GHz
0.091	0.034	0.033	0.021	0.039	-0.002	0.007	0.010	0.010	0.007	-0.002	0.015
0.034	0.067	0.037	0.018	0.029	0.012	0.003	0.005	0.005	0.005	0.010	-0.001
0.033	0.037	0.061	0.027	0.023	0.009	0.016	0.009	0.004	0.001	0.001	0.003
0.021	0.018	0.027	0.090	0.024	0.014	0.019	0.010	0.004	-0.005	0.004	-0.000
0.039	0.029	0.023	0.024	0.102	0.018	0.014	0.001	0.003	0.012	0.002	0.003
-0.002	0.012	0.009	0.014	0.018	0.058	0.003	0.004	-0.001	-0.002	0.003	0.001
0.007	0.003	0.016	0.019	0.014	0.003	0.051	0.002	0.003	0.006	-0.005	0.001
0.010	0.005	0.009	0.010	0.001	0.004	0.002	0.027	0.008	0.006	0.003	0.004
0.010	0.005	0.004	0.004	0.003	-0.001	0.003	0.008	0.019	0.001	0.006	0.006
0.007	0.005	0.001	-0.005	0.012	-0.002	0.006	0.006	0.001	0.082	0.013	0.003
-0.002	0.010	0.001	0.004	0.002	0.003	-0.005	0.003	0.006	0.013	0.066	0.003
0.015	-0.001	0.003	-0.000	0.003	0.001	0.001	0.004	0.006	0.003	0.003	0.040

For the low frequency channels, this is dominated by uncertainty on T_{ND} introduced by the calibration. There are significant off-diagonal terms, which will degrade the vertical resolution of the humidity profile that can be retrieved with these channels. Improving the quality control of the tip curve calibration would improve the overall noise on the water vapour channels by 0.02-0.03 K.

Summary of all Random Noise

The tip curve calibration is used to calculate T_{ND} for the water vapour channels, ≤ 30 GHz. Values of T_{ND} obtained from each tip curve are exponentially averaged before being applied to calibrate the radiometer's water vapour channels. This averaging reduces the theoretical noise by a factor of $\sim 1/\sqrt{20}$. However this averaging takes no account of the distribution of these tip curves in time. This should be improved in future releases of the processing software. The danger of averaging the tip curve calibrations in this way, is that genuine, high-frequency calibration changes may be attenuated.

Liquid Nitrogen calibrations are used to calculate T_{ND} for the oxygen channels > 50 GHz. In practise, several ($n \sim 20$) measurements of liquid nitrogen are averaged together (by hand!) to provide a single calibration for T_{ND} . This has the effect of reducing the total random noise by a factor of $1/\sqrt{n}$. However, in the time since the last calibration, random drift in T_{ND} will contribute to a changing bias in the radiometer signal.

Table 13 - Summary of Random Noise including Calibration

Frequency (GHz)	V2.14			v2.20		
	$NE\Delta T$ (K)	Noise on T_b using Tip (K)	Noise on T_b using LN2 (K)	$NE\Delta T$ (K)	Noise on T_b using Tip (K)	Noise on T_b using LN2 (K)
22.235	0.11	0.27	0.25	0.13	0.30	0.29
23.035	0.10	0.26	0.24	0.10	0.26	0.24
23.835	0.10	0.25	0.24	0.09	0.25	0.23
26.235	0.10	0.31	0.37	0.10	0.30	0.36
30.000	0.09	0.29	0.32	0.11	0.32	0.35
51.250	0.13	0.25	0.26	0.12	0.25	0.24
52.280	0.10	0.19	0.21	0.12	0.19	0.23
53.850	0.08	0.13	0.14	0.10	0.14	0.16
54.940	0.08	0.14	0.13	0.09	0.14	0.14
56.660	0.24	0.35	0.35	0.20	0.35	0.29
57.290	0.19	0.27	0.28	0.18	0.28	0.26
58.800	0.09	0.14	0.14	0.14	0.15	0.20

Table 13 summarises the r.m.s. noise in each radiometer channel using both versions of control software. The radiometric resolution, $NE\Delta T$, is the noise introduced by the radiometer itself. The other columns indicate the total noise, including that introduced by the tip curve and liquid nitrogen calibrations. These figures are taken from the error covariances, such as that presented in Table 12. The greyed figures indicate the values that would be obtained if the alternate calibration mechanism were used for each channel.

These figures are calculated from the statistics of the actual calibrations used during the trial at Camborne. They are similar to the modal variance of brightness temperatures measured using v2.20 over short periods (10 min), during stable conditions.

The total noise could be reduced to figures approaching the $NE\Delta T$ by changes to the processing software, as described above. However, even these figures are close to the resolution specified for the radiometer, 0.25 K [Radiometrics, 2001].

5. Systematic Errors (Bias)

Each term in the radiometer system equation (1) is potentially subject to systematic errors, which can bias the observed brightness temperature. This section evaluates each term, and summarises with a total expected bias for each channel in typical operating conditions. In principal, these biases can be corrected. However there is an uncertainty in the evaluation of each term. These uncertainties contribute directly to the overall error budget of the calibrated brightness temperatures and cannot be reduced by averaging. They are also evaluated for each term. The biases and their uncertainties are summarised in Table 20.

Black Body Temperature

The emissivity of this target is assumed to be 1—so its brightness temperature is equal to the thermodynamic temperature measured as the average of its 2 temperature sensors. In practise, it is likely that the emissivity of the target is limited by reflection of incident radiation from the surface of its insulating foam. However, this is a small effect. For example, if the emissivity is 0.99, 1% of the power received by the radiometer will be that emitted by the Gaussian Optics Antenna reflected by this surface. The temperature of this is likely to be within 1 K of the black body, which would not introduce a significant bias.

However, it is possible that signal from the local oscillator may ‘leak’ out through the mixer and isolator, and be reflected by the surface of the target or any other component in the optical path. Although this signal is nominally outside the passband of the receiver, it may be sufficient to cause interference in the mixer. This effect would introduce a constant bias in the apparent brightness temperature of the black body. It may be possible to test for this by placing a reflective plate in the view of the radiometer, and tracking its position slowly it through several wavelengths.

Otherwise, the accuracy of the brightness temperature of the black body target is limited by that of the temperature sensors. The data sheet quotes typical values of 0.3 °C for 0 – 70 °C. Radiometrics quote 0.2°C, which we shall take as the standard uncertainty in T_{bb} . This has a direct and linear impact on the final brightness temperatures (Equation (1)).

T_{ND} derived from Tip Curve Calibrations

Both calibration mechanisms can introduce bias on noise diode brightness temperature. This section assesses the bias introduced by the tip curve calibration. This is expressed in terms of a bias in the retrieved zenith brightness temperature, but this can be projected to calculate the corresponding bias on T_{ND} , using Equation (1).

Han & Westwater [2000] analysed the tip curve calibration process and identified contributions to the error budget from a number of sources. They evaluated these terms for a particular radiometer in continental conditions. These (and others) are evaluated here based on the data from the trial of the radiometer at Camborne.

Tip Curve – Mean Radiative Temperature, T_{mr}

The Mean Radiative Temperature, T_{mr} is used in the tip curve calibration to convert between brightness temperatures and opacity in Equation (3). At present a constant value of T_{mr} is prescribed for each channel. This is clearly a simplification, and will introduce a bias that will vary a little with atmospheric conditions.

Ideally, T_{mr} should be calculated from the radiative transfer equation. However, for optically thin channels, we can approximate the calculation of T_{mr} as the average temperature, T , of the profile weighted by the water vapour density, ρ_{wv} :

$$T_{mr} \approx \frac{\int_0^{\infty} T(z) \cdot \rho_{wv}(z) \cdot dz}{\int_0^{\infty} \rho_{wv}(z) \cdot dz} \quad (12)$$

This is evaluated for all the clear radiosonde profiles from Camborne, and was found to have an average annual value of $T_{mr}=275.2$ K with a standard deviation of 3.6 K. This is close to the value prescribed in the software. A simple model can be used to reduce the variance in T_{mr} by parameterizing it in terms of the ambient temperature, T_{amb} : $T_{mr}=T_{amb}+8.5$ with a standard deviation of 2.9 K.

By perturbing the nominal value of T_{mr} by an amount equivalent to its variance it is possible to assess its impact on the retrieved zenith brightness temperature. Results of this calculation are shown in Table 16. This shows that uncertainty in T_{mr} introduces a negligible bias in the tip curve calibrations for the optically thin water vapour channels. However, if the tip curve technique were to be applied to the low frequency oxygen channels, this would become the dominant source of uncertainty in the calibration.

Tip Curve – Cosmic Microwave Background

There are two definitions of brightness temperature commonly used in microwave remote sensing: the *thermodynamic brightness temperature* and the *Rayleigh-Jeans equivalent brightness temperature* [Janssen, 1993]. In the tip curve calibration we use the Rayleigh-Jeans equivalent brightness temperature, but this approximation is not valid for very low brightness temperatures (or high frequencies). To compensate for this, a correction is commonly applied to the brightness temperature of the cosmic microwave background, T_c to give the *Rayleigh-Jeans equivalent brightness temperature*, T_{cmb} :

$$T_{cmb} = \frac{h\nu}{2k} \left(\frac{e^{\frac{h\nu}{kT_c}} + 1}{e^{\frac{h\nu}{kT_c}} - 1} \right) \quad (13)$$

where $h=6.626176e-34$ J.s, $k=1.380662e-23$ J/K, $T_c=2.736$ K, ν =frequency (Hz).

Equation (13) is evaluated at the centre frequency of each channel of the radiometer in Table 14. At present the software prescribes the same value (2.73K) to all channels. This introduces a small bias (0.06 K) on the zenith brightness temperature retrieved by the tip curve at 30 GHz. This bias would increase if the tip curve were applied to higher frequencies. As this bias is constant, it is not included in the further analysis.

Table 14 - Effective Brightness Temperature of Cosmic Microwave Background

Freq.	22.235	23.035	23.835	26.235	30.000	51.250	52.280	58.850	54.940	56.660	57.290	58.800 GHz
Tcmb	2.771	2.773	2.776	2.784	2.799	2.918	2.925	2.975	2.945	2.958	2.962	2.974 K

Tip Curve – Beamwidth Correction

A microwave radiometer does not have an infinitesimal beamwidth, but integrates emission over a range of azimuth and elevation angles. As the sky brightness temperature, T_b , increases at low elevation angles, the measured antenna temperature will be higher than that modelled for an infinitesimal beam. If not corrected, this can introduce a bias in the tip curve calibrations.

The current operational software applies a correction similar to that derived in Appendix 1 of Han & Westwater [2000]:

$$T_a(\theta) = T_z(\theta) + \frac{FWHM^2}{16 \cdot \ln(2)} \cdot (T_{mr} - T_{cmb}) \cdot e^{-\tau(\theta)} \cdot \left[2 + \frac{2 - \tau(\theta)}{\tan(\theta)^2} \right] \cdot \tau(\theta) \quad (14)$$

where $T_a(\theta)$ is the antenna temperature at elevation angle, θ ; $T_z(\theta)$ is the sky brightness temperature;
 T_{mr} is the mean radiative temperature,
 T_{cmb} is the brightness temperature of the cosmic microwave background;
 τ is the opacity,
 $FWHM$ is the Full Width Half-Maximum beamwidth.

These corrections are proportional to the zenith opacity, but are generally small (<0.1 K). This term grows exponentially for elevation angles lower than 30°, which are best avoided in tip curves. This correction is evaluated to investigate the uncertainty introduced by an uncertainty of ±15% in the beamwidth, $FWHM$. Table 16 shows the impact of this bias on retrieved zenith brightness temperature is largest at low frequencies (0.12 K), and has a small uncertainty.

Tip Curve – Effect of Atmospheric Refractive Index

The vertical gradient of refractive index causes the slant path at low elevation angles to differ from that assumed in the tip curve. Under normal conditions, the beam is bent downwards and introduces a bias in the tip curve calibration. However, Han & Westwater [2000] show that this term is typically negligible (<0.01 K) for elevation angles $\theta \geq 19.5^\circ$. This is not currently corrected in the operational code, so the uncertainty on this term is assumed to be ±50%, but is negligible as shown in Table 16.

Tip Curve – Effect of Earth Curvature

The Earth's curvature causes the slant path at low elevation angles to be smaller than in the atmosphere of a flat Earth. This term has a larger effect than the refractive index. Han & Westwater [2000] give this expression for the slant path, a at elevation angle, θ :

$$a = \sec \theta - H \cdot \sec \theta \cdot (\sec^2 \theta - 1) / r_e \quad (15)$$

where $r_e=6370.95$ is the radius of the Earth,
 H is the effective (scale) height for atmospheric emission, $H \sim 2.0 \pm 0.4$ km for the window (water vapour) channels. $H \sim 8 \pm 2$ km for the oxygen channels.

The impact of this bias on the zenith brightness temperature retrieved by the tip curve is shown in Table 16. Also shown is the uncertainty associated with the variance in H . The magnitude of this bias is proportional to the atmospheric opacity, and is negligible for optically thin channels, as is the uncertainty in this term.

This is not currently corrected in the operational code, but is a small term for the current configuration. However, if tip includes 19.5° elevation angles, it becomes significant, but only for the oxygen band channels, where the tip curve is not used at present. This is shown in Table 17.

Tip Curve – Beam pointing

If the radiometer beam is systematically misaligned in elevation, a bias will be introduced in the tip curve calibration. However, the current configuration minimises this bias, as the angles used for the tip curve are symmetric about zenith. The instrument is believed to be horizontally aligned within 1°. As shown in Table 16, the resulting bias in the retrieved zenith

brightness temperature is very small ≤ 0.02 K, regardless of the range of tip angles used, so long as they are symmetric about zenith.

If tip curve measurements are only made on one side of zenith, substantial errors can be introduced in the retrieved zenith brightness temperature (e.g. $\Delta T_z = 0.3$ K for 23.8 GHz using only $\theta = 30^\circ, 45^\circ, 90^\circ$)

Tip Curve – Systematic Atmospheric Asymmetry

A systematic gradient in humidity over the radiometer site along the direction of the tip curve elevation scan will introduce a bias in the calibration. This may be the case at Camborne at certain times of year, due to the contrast in humidity over the sea and land. It is, however, very difficult to quantify.

Analysis of the brightness temperatures measured at each angle of the tip curve throughout the trial reveals a small, systematic difference between views on opposite sides of zenith. However, it was found that this difference could be explained by a simple beam pointing error of only $\sim 0.15^\circ$. This is well within the uncertainty of the alignment, so remains the most likely explanation. The systematic component of the non-stratified term is therefore assumed to be completely negligible.

Tip Curve – Changes in Mirror Reflectivity

No mirror is perfect. As the mirror rotates, the polarisation angle incident on it also rotates. And the reflectivity of the mirror varies with polarisation angle. This mechanism can introduce a bias in the brightness temperatures measured in all views, including the calibration views.

The radiometer views the black body target and the observed scenes via a rotating mirror. Thermal emission by the mirror biases each view by:

$$\Delta T_b(\vartheta) = (1 - \Gamma(\vartheta)) \cdot (T_{MIR} - T_b) \quad (16)$$

where T_b = brightness temperature of the scene 'before' reflection,
 T_{MIR} = temperature of the mirror (assumed to be the same as the black body),
 Γ = mirror reflectivity, which varies as a function of the angle of polarisation ϑ as:

$$\Gamma(\vartheta) = \Gamma_{//} \cdot \cos^2(\vartheta) + \Gamma_{\perp} \cdot \sin^2(\vartheta) \quad (17)$$

Here, $\Gamma_{//}$ and Γ_{\perp} are the power reflectivities of the mirror for parallel and perpendicularly polarised radiation, which are constant for a given wavelength for a plane mirror set at a constant inclination. They can be calculated from Fresnel's Equations (18):

$$\Gamma_{//}(\nu) = \left| \frac{Z_2(\nu) - Z_1 \cos(\psi)}{Z_2(\nu) + Z_1 \cos(\psi)} \right|^2 \quad (18)$$

$$\Gamma_{\perp}(\nu) = \left| \frac{Z_2(\nu) \cos(\psi) - Z_1}{Z_2(\nu) \cos(\psi) + Z_1} \right|^2$$

where ψ is the angle of incidence on the mirror (in this case 45°),
 Z_1 is the impedance of free space (377Ω),
 $Z_2(\nu)$ is the impedance of the mirror at frequency, ν , given by equation (19):

$$Z_2(\nu) = \frac{1+i}{\sigma \cdot \delta(\nu)} \quad (19)$$

Where σ is the surface conductivity of the mirror, and $\delta(\nu)$ is the penetration depth:

$$\delta(\nu) = \sqrt{\pi \cdot \sigma \cdot \nu \cdot \mu} \quad (20)$$

where μ is the permeability of free space, $\mu = 4\pi \cdot 10^{-7} \text{ Hm}^{-1}$. The radiometer mirror has a flat surface of polished aluminium 6061-T6, which has a conductivity of $\sigma = 1.2 \times 10^7 \text{ S.m}^{-1}$ [Lamb, 1996, Ref (73)]. There was typo in the figure for stainless steel quoted in Table 2 of [McGrath & Hewison, 2001] – it should read $\sigma = 1.8 \times 10^6 \text{ S.m}^{-1}$.

The radiometer views the black body and the zenith in the same polarisation angle, ϑ . Thus the reflectivity of the mirror is the same in each of these views, and any thermal emission is cancelled out in the calibration. However, during the tip curve, the polarisation angle incident on the mirror changes with elevation angle.

A view dependent bias is introduced by the mirror's reflectivity changing with polarisation (and hence scan) angle. This can produce a bias in the tip curve calibration of $\sim 0.2 \text{ K}$ for the 30 GHz channel in clear skies ($T_b = 15\text{K}$), which is a worst case. Incidentally, the magnitude of this bias is almost the same for the 51.25 GHz channel. Although the frequency is higher, the zenith brightness temperatures are closer to the mirror temperature, and the polarisation angles are orthogonal. The magnitude of the bias reduces by $\sim 15\%$ when elevation angles of (19.5°, 30°, 90°, 150°, 160.5°) are used instead of (30°, 45°, 90°, 135°, 150° and 90°).

This bias is not corrected for in the current processing software.

The dominant source of uncertainty in this term is due to the uncertainty in the mirror's conductivity. This is estimated to $\pm 50\%$, based on the variation of published data from different sources. This results in an uncertainty in this bias term of $\pm 33\%$. The polarisation angle is known to within a few degrees, and this makes no difference to the bias.

Tip Curve – Beam Efficiency/Sidelobes

An important factor that was not included in the analysis of Han & Westwater [2000] is the contamination due to antenna sidelobes being exposed to contrasting scenes. The most contrasting scene is ground emission, which will be most exposed at lower elevation angles. It is, however, very difficult to quantify or correct. This section attempts to estimate the magnitude of the uncertainty of this bias.

The antenna temperature, T_a , measured by the radiometer is the integral of the scene brightness temperature, $T_b(\theta, \phi)$, multiplied by the antenna gain, $g(\theta, \phi)$: [Janssen, 1993]

$$T_a = \int_{4\pi} g(\theta, \phi) T_b(\theta, \phi) d\Omega \quad (21)$$

To evaluate this expression, it is necessary to have accurate knowledge of the antenna gain over the full hemisphere. This is not available for most radiometers, so here we simplify this expression by introducing the concept of beam efficiency.

We define the beam efficiency, η , as the fraction of received power that originated with an cone of half angle, Θ , of the beam's boresight. It is assumed that the remaining power is distributed evenly over the rest of the hemisphere, and that there is no sensitivity in the backward direction. As the elevation angle, θ , is reduced from zenith, the solid angle exposed to the ground, Ω_{GND} , increases as:

$$\Omega_{GND}(\theta) = |\pi \cdot \cos \theta| \quad (22)$$

The modelled performance of a similar corrugated feedhorn antenna has a beam efficiency, $\eta \sim 99.9\%$ within a half angle of 30° and $\eta \sim 99.64\%$ within 20° [Pat Foster, MAAS, Personal Communication 23/1/03].

The contribution, ΔT_b , from this solid angle exposed to a scene contrast, ($T_{GND} - T_b$) is:

$$\Delta T_b(\theta) = (1 - \eta) \cdot \frac{\Omega_{GND}(\theta)}{2\pi - \Omega_{WB}} [T_{GND} - T_b(\theta)] \tag{23}$$

This represents a systematic bias, which is not currently corrected in the processing. The magnitude of the bias will vary with angle systematically from one channel to another, and be proportional to the contrast between the brightness temperature of the sky and the ground.

It is possible to estimate the magnitude of these terms indirectly by comparing calibrations derived from different sets of tip curve angles. In this case, comparing calibrations from the good conditions on the morning of 14 February 2003 using tip angles set *a* ($19.5^\circ, 30^\circ, 90^\circ, 150^\circ, 160.5^\circ$) and set *b* ($30^\circ, 45^\circ, 90^\circ, 135^\circ, 150^\circ$ and 90°).

Both sets of angles give similar, *low* levels of random noise on the retrieved value of T_{ND} , making it easy to identify the systematic difference between them. The difference is largest at the lowest frequency, where the beamwidth is broadest, and theoretically the sidelobes will be worst for a given aperture truncation. This difference is ~ 12 times larger than that predicted from using the modelled beam efficiencies above. This suggests the beam efficiency $\eta \sim 95.5\%$ within $\pm 20^\circ$. Presumably, the value corresponding to $\pm 30^\circ$ would scale linearly to $\eta \sim 99.0\%$. The results are shown in Table 15.

**Table 15 – Estimating the Beam Efficiency within $\pm 30^\circ$ and $\pm 20^\circ$ from Tip Curve Calibrations with different sets of elevation angles.
(a)= ($19.5^\circ, 30^\circ, 90^\circ, 150^\circ, 160.5^\circ$) and (b)= ($30^\circ, 45^\circ, 90^\circ, 135^\circ, 150^\circ$ and 90°)**

Frequency (GHz)	Tnd Tip Curve Angles (a) (K)	Tnd Tip Curve Angles (b) (K)	Tnd Difference (b)-(a) (K)	Tb Nominal Difference (a)-(b) (K)	Beam Efficiency + 20 deg (%) from (a)	Beam Efficiency + 30 deg (%) from (b)
22.235	324.06 ± 0.36	325.88 ± 0.35	1.82 ± 0.08	1.45 ± 0.06	95.50 ± 0.20	99.00 ± 0.04
23.035	319.62 ± 0.33	320.96 ± 0.35	1.33 ± 0.08	1.07 ± 0.06	96.75 ± 0.20	99.29 ± 0.04
23.835	318.85 ± 0.27	320.11 ± 0.29	1.26 ± 0.07	1.03 ± 0.06	96.75 ± 0.18	99.29 ± 0.04
26.235	187.86 ± 0.20	188.33 ± 0.21	0.47 ± 0.05	0.67 ± 0.07	98.00 ± 0.21	99.58 ± 0.04
30.000	210.50 ± 0.23	210.68 ± 0.23	0.18 ± 0.05	0.23 ± 0.06	99.35 ± 0.18	99.90 ± 0.03

The impact of this bias on the retrieved zenith brightness temperature is shown in Table 16. For the current operational configuration for tip curves using elevation angles (a) of $30^\circ, 45^\circ, 90^\circ, 135^\circ, 150^\circ$ and 90° , the bias is typically 0.5 K at 22.235 GHz, the most effected channel. Using lower elevation angles (b) in the tip curve, increases this bias by a factor of 4, as shown in Table 17.

The uncertainty on this term is very large. The beam efficiency is unknown and very difficult to measure with an accuracy of better than 0.5%. The beam efficiency used is based on these calculations has an estimated uncertainty of 100%. This term then dominates the uncertainty in the overall budget of systematic errors for the tip curve calibration.

Tip Curve – Summary of Systematic Errors

Table 16 and Table 17 summarises the bias introduced by the tip curve calibration by the above mechanisms. These are expressed as the mean bias on retrieved nominal zenith brightness temperatures for clear skies, and their standard uncertainties. For both combinations of elevation angle, the dominant source of bias and uncertainty is due to low beam efficiency, or *Sidelobe contamination*.

**Table 16 - Summary of Tip Curve Systematic Errors and their Uncertainties.
Based on Software v2.14 and v2.20, using Elevation Angles 30°, 45°, 90°, 135°, 150°, 90°**

Freq (GHz)	Refractive Index Changes (K)		Earth Curvature (K)		Bias due to mirror reflectivity (K)		Uncertainty in Mean Radiative Temperature (K)		Beamwidth Correction (K)		Sidelobe Contamination (K)		Beam Pointing Error (K)		Total Systematic Bias (K)	
22.235	0.01 ±	0.00	-0.01 ±	-0.01	0.17 ±	0.05	0.00 ±	0.01	0.12 ±	0.04	0.48 ±	0.48	0.00 ±	0.00	0.76 ±	0.48
23.035	0.01 ±	0.00	-0.01 ±	-0.01	0.18 ±	0.05	0.00 ±	0.01	0.10 ±	0.03	0.35 ±	0.35	0.00 ±	0.00	0.62 ±	0.35
23.835	0.01 ±	0.00	-0.01 ±	-0.01	0.18 ±	0.05	0.00 ±	0.01	0.08 ±	0.03	0.35 ±	0.35	0.00 ±	0.00	0.60 ±	0.35
26.235	0.01 +	0.00	-0.01 +	-0.01	0.19 +	0.05	0.00 +	0.01	0.05 +	0.02	0.20 +	0.20	0.00 +	0.00	0.44 +	0.20
30.000	0.01 ±	0.00	-0.01 ±	-0.01	0.22 ±	0.06	0.00 ±	0.00	0.04 ±	0.01	0.05 ±	0.05	0.00 ±	0.00	0.31 ±	0.08
51.250	0.02 ±	0.01	-0.16 ±	0.04	0.24 ±	0.08	0.08 ±	0.27	0.05 ±	0.01	0.03 ±	0.03	0.00 ±	0.01	0.26 ±	0.29
52.280	0.03 ±	0.01	-0.19 ±	0.05	0.21 ±	0.07	0.23 ±	0.75	0.05 ±	0.02	0.03 ±	0.03	0.00 ±	0.02	0.34 ±	0.76
53.850	0.05 ±	0.02	-0.13 ±	0.03	0.15 ±	0.05	0.45 ±	1.50	-0.02 ±	0.01	0.02 ±	0.02	0.00 ±	0.01	0.52 ±	1.50

**Table 17 - Summary of Tip Curve Systematic Errors and their Uncertainties
Based on Software v2.20, using Elevation Angles 19.5°, 30°, 90°, 150°, 160.5°**

Freq (GHz)	Refractive Index Changes (K)		Earth Curvature (K)		Bias due to mirror reflectivity (K)		Uncertainty in Mean Radiative Temperature (K)		Beamwidth Correction (K)		Sidelobe Contamination (K)		Beam Pointing Error (K)		Total Systematic Bias (K)	
22.235	0.03 ±	0.01	-0.03 ±	0.01	0.14 ±	0.04	0.00 ±	0.02	0.20 ±	0.07	1.95 ±	1.95	0.00 ±	0.00	2.28 ±	1.95
23.035	0.03 ±	0.01	-0.03 ±	0.01	0.15 ±	0.04	0.00 ±	0.02	0.17 ±	0.06	1.41 ±	1.41	0.00 ±	0.00	1.72 ±	1.41
23.835	0.03 ±	0.01	-0.03 ±	0.02	0.15 ±	0.04	0.00 ±	0.02	0.16 ±	0.05	1.41 ±	1.41	0.00 ±	0.00	1.71 ±	1.41
26.235	0.02 +	0.01	-0.02 +	0.00	0.16 +	0.04	0.00 +	0.01	0.12 +	0.03	0.86 +	0.86	0.00 +	0.00	1.14 +	0.86
30.000	0.02 ±	0.01	-0.02 ±	0.00	0.17 ±	0.04	0.00 ±	0.01	0.07 ±	0.02	0.28 ±	0.28	0.00 ±	0.00	0.52 ±	0.28
51.250	0.10 ±	0.05	-0.44 ±	0.22	0.21 ±	0.05	0.19 ±	0.57	0.07 ±	0.02	0.14 ±	0.14	0.00 ±	0.00	0.26 ±	0.63
52.280	0.14 ±	0.07	-0.54 ±	0.27	0.18 ±	0.05	0.61 ±	1.82	0.03 ±	0.01	0.11 ±	0.11	0.00 ±	0.00	0.52 ±	1.84
53.850	0.23 ±	0.11	-0.34 ±	0.17	0.13 ±	0.03	1.21 ±	3.64	-0.16 ±	0.05	0.08 ±	0.08	0.00 ±	0.00	1.15 ±	3.65

Resulting uncertainties shown in Table 17 are much higher than those shown in Table 16, primarily due to the increase in sidelobe contamination. It is therefore recommended that tip curves are restricted to elevation angles greater than 30°, and that future designs for radiometer quasi-optics prevent beam truncation to ensure higher beam efficiencies.

T_{ND} derived from Liquid Nitrogen Calibrations

A liquid nitrogen target is used to provide an absolute reference scene for the calibration of the noise diode brightness temperature for use with the optically thick oxygen channels.

Each component of the liquid nitrogen calibration target is analysed here, to calculate its contribution to the overall brightness temperature by emission, or absorption (and even scattering!). These terms are summarised in Table 18.

Liquid Nitrogen – Emission by absorber

The heart of the calibration target is a layer of permeable microwave absorber, immersed in liquid nitrogen. The cryogen is assumed to be isothermal at the boiling point of nitrogen at atmospheric pressure, incremented a little to account for the hydrostatic pressure due to a 20 cm column of liquid nitrogen. This is 77.55 K at 1013 hPa, but varies by ± 0.2 K over the typical range of pressures experienced at Camborne. These corrections are accounted for in the processing software.

The microwave absorber is assumed to be a perfect black body with an emissivity of 1. This is a good approximation, as similar material has reflectivity < -40 dB, which would give an bias of < 0.02 K.

Liquid Nitrogen – reflections in the LN2-polystyrene interface

The liquid nitrogen is contained in a box of expanded polystyrene foam. The dissimilar dielectric properties of these materials cause some of the radiation incident at the interface to be reflected.

The nominal density of solid polystyrene (from Kaye & Laby) is $d_0 = 1050 \text{ kg m}^{-3}$
The density of the foam currently used in Radiometrics target is $d = 27.8 \text{ kg m}^{-3}$ (1.75 lb/ft³).

According to Sanford [1995], the dielectric constant of the foam, ϵ_r is:

$$\epsilon_r = \frac{2}{5} \epsilon_{r0}^{d/d_0} + \frac{3}{5} \left[1 + \frac{d}{d_0} (\epsilon_{r0} - 1) \right] \quad (24)$$

Where $\epsilon_{r0} = 2.54$ is the dielectric constant of solid polystyrene [Lamb, 1996 ref (24)].

The reflectivity of the interface is:

$$\Gamma = \frac{\left| \sqrt{\epsilon_{LN2}} - \sqrt{\epsilon_{Polystyrene}} \right|^2}{\left| \sqrt{\epsilon_{LN2}} + \sqrt{\epsilon_{Polystyrene}} \right|^2} \quad (25)$$

Where ϵ_{LN2} is the dielectric constant of liquid nitrogen. $\sqrt{\epsilon_{LN2}} = 1.196$ at $\lambda = 2.3 \text{ mm}$ [Vinogradov *et al.*, 1967]. This results in a power reflectivity of planar LN2-polystyrene interface to be 0.0066, which would increase the brightness temperature of the target by 1.44 K.

However, it is believed that liquid nitrogen gradually penetrates between the beads of polystyrene and breaks down the interface. This effect reduces the magnitude of this term by an unknown amount. The brightness temperature of the target has been observed to reduce by ~ 1 K during the first few minutes after filling [Hewison & McGrath, 2001]. It will, therefore be assumed that this term has a negligible contribution for low-density polystyrene targets (1.75 lb/ft³). A correction of 1.7 K due to this term is included in the processing software. There remains a large uncertainty on this term.

Liquid Nitrogen – polystyrene emission

Lamb [1996] reports a number of measurements of solid polystyrene loss tangents, $\tan \delta$, at millimetre wavelengths, which show consistent frequency dependence of the form:

$$\tan \delta = 0.98 \cdot 10^{-3} + 6.01 \cdot 10^{-6} \nu \quad (26)$$

where ν is the frequency in GHz. $\tan \delta$ is the ratio of imaginary to real parts of permittivity.

We assume that the imaginary part of the dielectric constant scales linearly with foam density. So, the power attenuation coefficient, α [m^{-1}], can be calculated as:

$$\alpha = \frac{2\pi\sqrt{\epsilon} \cdot \nu \cdot \tan \delta}{c} \quad (27)$$

where ν is the frequency in Hz, c is the speed of light in vacuum.

While absorbing incident radiation, thermal emission by the polystyrene also contributes to the scene brightness temperature. However, the temperature profile through the absorber is unknown. As we know the surface of the box is only a few degrees cooler than ambient after several hours of use, we approximate its average temperature as being ambient.

Table 18 shows the net contribution from the polystyrene increases with frequency from 0.4 K at 22.235 GHz to 1.2 K at 58.8 GHz. The uncertainty on this term is estimated as $\pm 50\%$. This increases with higher density foams.

Although a correction is applied in the software that processes the liquid nitrogen calibrations, it is a factor of ~ 4 smaller than these figures, and should be revised. This tends to cancel out part of the interface reflection term, which is believed to be overestimated at present.

Liquid Nitrogen – polystyrene scattering loss

The beads of polystyrene foam are estimated to be 2 mm in diameter, i.e. of the same order as the wavelengths of the highest frequency channels. This is the regime in which volume scattering is most efficient. Anthony Baran has modelled the scattering cross section of polystyrene beads of 1, 2 and 3 mm diameters with the above dielectric characteristics. His calculations are used to predict the extinction by the base of the polystyrene box, shown in Table 18. The results show scattering is a small, but significant contribution at the highest frequencies.

Liquid Nitrogen – polystyrene-polyethylene-air interface reflection

A $\frac{1}{4}$ " layer of high-density polyethylene foam (HDPE) is attached to the underside of the polystyrene target to act as a thermal barrier to prevent the formation of condensation. This has very similar dielectric properties to polystyrene and air, so no significant reflections are expected at these interfaces. This foam is fixed to the base of the polystyrene by tape. The gap between it and the polystyrene was found to fill with nitrogen gas, which ensures it is kept free of condensation.

Liquid Nitrogen – polyethylene emission

The loss tangent of this HDPE foam can be calculated from its solid properties using Equations (24) to (27) using figures from Lamb [1996, ref(36)]. These predict negligible loss due to the foam.

Liquid Nitrogen – Summary of Systematic Errors

Table 18 summarises the contribution of each component of the liquid nitrogen calibration target to its brightness temperature. The total of these terms is shown to increase from 0.43 K to 1.61 K from the lowest to highest frequencies. This is comparable to the correction currently applied in the processing software. The uncertainty on these terms is dominated by the reflections at the LN2-polystyrene interface. At present, the standard uncertainty of 0.4 K is prescribed to this. This could be reduced by experimentation in the lab.

Table 18 - Systematic Errors in Brightness Temperature of Liquid Nitrogen Target, with polystyrene density 1.75 lb/ft³

Frequency, f	22.235	23.8	30	51.25	52.28	53.85	58.8	GHz
HDPE Absorption Loss	0.02	0.02	0.02	0.02	0.02	0.02	0.02	K
HDPE Scattering Loss	0.00	0.00	0.00	0.00	0.00	0.00	0.00	K
Reflection at HDPE-air interface	0.01	0.01	0.01	0.01	0.01	0.01	0.01	K
PS Absorption Loss	0.39	0.42	0.55	1.05	1.07	1.11	1.24	K
PS Scattering Loss	0.00	0.00	0.01	0.04	0.10	0.24	0.33	K
Reflection at HDPE-PS interface	0.00	0.00	0.00	0.00	0.00	0.00	0.00	K
Reflections at PS-LN2 interface	1.39	1.39	1.39	1.39	1.39	1.39	1.39	K
Total Extinction modelled (excluding PS-LN2 interface)	0.43	0.46	0.59	1.12	1.21	1.39	1.61	K

Detector Non-Linearity

Implicit in the use of a 2-point calibration is the assumption that the radiometer output is linear with input power over the range between the scene and calibration points. In reality, the detector diode introduces a non-linearity, which produces a bias over certain values of scene brightness temperature. This bias is largest at points furthest from the calibration references.

Radiometrics are developing a 4-point calibration system to incorporate a non-linear correction. This will be available in a future software release. In tests, this bias varies by an order of magnitude between different channels of different instruments, but is expected to remain constant for each channel.

If liquid nitrogen and ambient calibration points are used, for scene brightness temperatures in the range between the calibration points, at $T_b \sim 200$ K, the bias varies from -0.1 to -0.7 K. The error is largest as $T_b \rightarrow 0$ K, and can be +0.25 to +1.25 K. However, the water vapour channels are calibrated using the tip curve, which provides a reference point within the observed range of brightness temperatures. This will reduce the bias in these channels to negligible levels in clear skies.

Table 20 gives estimates of the impact of the non-linearity measured for other Radiometrics instruments on scenes of nominal brightness temperatures. These biases could be corrected if the non-linearity was measured for our instrument. The uncertainties in Table 20 represent the variance of the non-linearity between different channels of different instruments. These uncertainties would become negligible if this were measured during liquid nitrogen calibrations.

Temperature Dependence of T_{ND}

The radiometer's calibration is found to vary with ambient temperature. The values of T_{ND} derived from the calibrations are archived for a nominal (black body) temperature of 290 K. When these values are applied to calibrate the radiometer through Equation (1), a linear temperature correction is applied based on fixed temperature coefficients measured by Radiometrics.

However, it is found that there is a residual dependence of T_{ND} with ambient temperature, as shown in the upper panels of Figure 6. These results are summarised in Table 19.

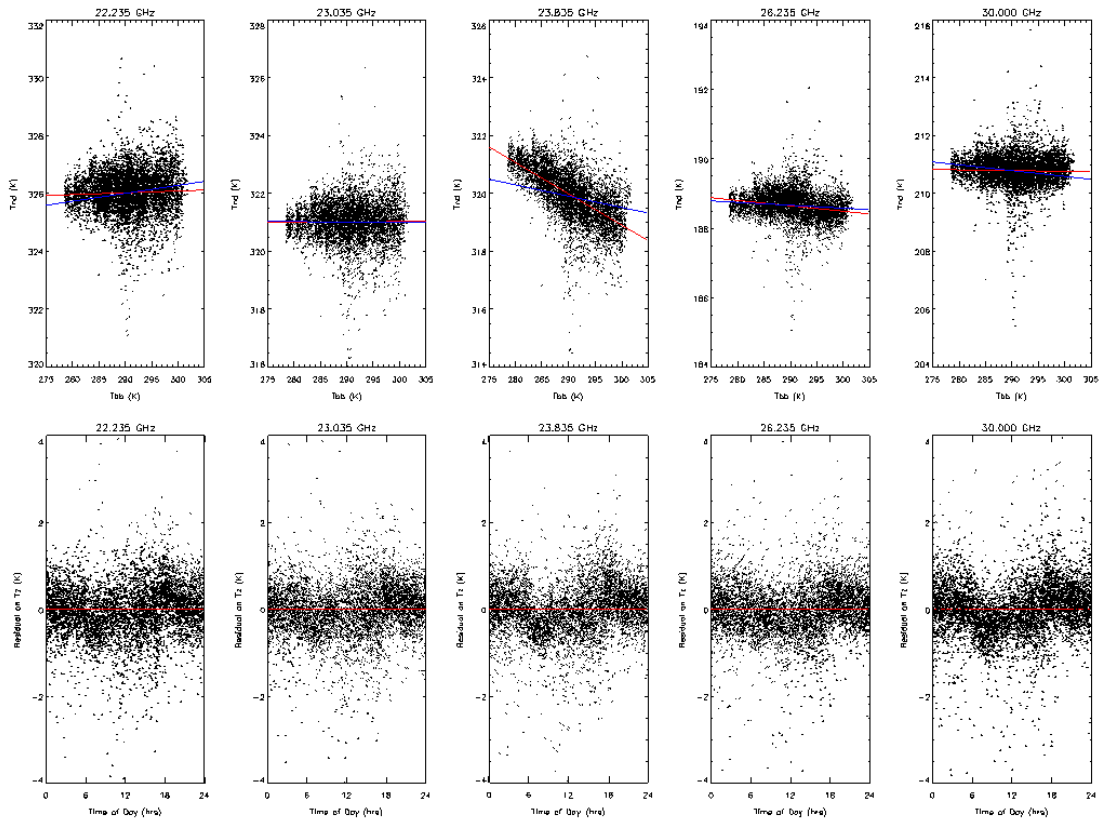


Figure 6 – Upper panels: T_{ND} with nominal temperature coefficient (blue). Lower panels: residuals on T_z after subtracting revised temperature coefficients (red). Data from Cardington Trial 19/3/03 – 9/4/03.

Table 19- Statistics from upper panels of Figure 6

Frequency (GHz)	T_{ND} at 290 K (K)	New Coeff (K/K)	Current Coeff (K/K)	r.m.s. (K)	r.m.s. from Exp Ave (K)
22.235	326.05	+0.0062	+0.027	0.74	0.34
23.035	321.05	+0.0012	-0.002	0.70	0.32
23.835	320.02	-0.1072	-0.039	0.71	0.37
26.235	188.69	-0.0154	-0.008	0.40	0.19
30.000	210.82	-0.0027	-0.020	0.53	0.26

New temperature coefficients are fitted to the variation of T_{ND} with black body temperature. These are shown in the 3rd column of Table 19, and should be applied *instead of* those already applied (shown in the 4th column).

The lower panels of Figure 6 show that even after applying the new correction, T_{ND} dips around dawn for all channels. This is broadly similar for all channels (when projected to zenith brightness temperature), and shows an increase with frequency, consistent with absorption by liquid water on the microwave window. However, this anomalous behaviour occurs at the time of maximum temperature changes, and is believed to be due to contributions from radiometer components, such as the microwave window, at temperatures between ambient and the black body with variable thermal lags.

The r.m.s. residuals on T_{ND} after the revised temperature correction are given in the last 2 columns of Table 19. The lower frequencies are very similar to those given in Table 5. However, there has been a dramatic improvement at the 26 & 30 GHz.

Summary of all Systematic Errors

Table 20 shows the total bias introduced in observations at nominal scene brightness temperatures for the current configuration of liquid nitrogen and tip curve calibrations. This shows that the tip curve introduces lower uncertainties for the lowest frequencies. At the higher frequencies where the atmosphere is optically thick, liquid nitrogen is better, as the tip curve becomes unfeasible.

Table 20 - Summary of all Contributions to Systematic Error Budget from Liquid Nitrogen and Tip Curve Calibrations

Frequency (GHz)	Bias on Black Body (K)	Bias on T_b Liquid Nitrogen (K)	Non-linearity on T_b from LN2 Cal (K)	Bias on T_b Tip Curve (K)	Total Bias on Nominal T_b from LN2 (K)	Total Bias on Nominal T_b from Tip Curve (K)
22.235	0 ± 0.20	0.43 ± 0.59	0.48 ± 0.23	0.76 ± 0.48	1.12 ± 0.80	0.76 ± 0.52
23.035	0 ± 0.20	0.45 ± 0.60	0.49 ± 0.23	0.62 ± 0.35	1.15 ± 0.82	0.62 ± 0.40
23.835	0 ± 0.20	0.46 ± 0.61	0.52 ± 0.24	0.60 ± 0.35	1.22 ± 0.84	0.60 ± 0.40
26.235	0 ± 0.20	0.51 ± 0.65	0.58 ± 0.28	0.44 ± 0.20	1.40 ± 0.92	0.44 ± 0.29
30.000	0 ± 0.20	0.59 ± 0.71	0.60 ± 0.29	0.31 ± 0.08	1.54 ± 1.01	0.31 ± 0.21
51.250	0 ± 0.20	1.12 ± 1.19	-0.20 ± -0.10	0.26 ± 0.29	0.80 ± 1.06	0.26 ± 0.35
52.280	0 ± 0.20	1.21 ± 1.28	-0.40 ± -0.20	0.35 ± 0.76	0.55 ± 0.89	0.35 ± 0.78
53.850	0 ± 0.20	1.39 ± 1.45	-0.40 ± -0.20	0.52 ± 1.50	0.22 ± 0.38	0.52 ± 1.52
54.940	0 ± 0.20	1.44 ± 1.49	-0.10 ± -0.05		0.11 ± 0.24	
56.660	0 ± 0.20	1.51 ± 1.57	-0.05 ± -0.03		0.09 ± 0.22	
57.290	0 ± 0.20	1.54 ± 1.59	-0.03 ± -0.01		0.09 ± 0.22	
58.800	0 ± 0.20	1.61 ± 1.66	-0.01 ± -0.01		0.10 ± 0.22	

The average bias presented in Table 20 can be corrected in the processing software. However, there will always be a residual uncertainty attached to this, which limits the overall accuracy of the radiometer's brightness temperature measurements. This can be reduced by improving our understanding of the tip curve and liquid nitrogen calibrations.

In particular, the interface between the liquid nitrogen and the polystyrene should be investigated. This may be possible by comparing measurements of the current target, and one with a membrane of thin HDPE sheet to prevent the liquid nitrogen from penetrating into the polystyrene. Also, the insertion loss of the base of the polystyrene box could be characterised by measuring the target's brightness temperature through a number of additional layers of polystyrene of the same density. Although this has been attempted in the field, it would be better performed in the lab, with more stable conditions, faster observing cycle and more samples of polystyrene available.

The uncertainty due to detector non-linearity will be reduced to negligible levels when this parameter is explicitly measured during the liquid nitrogen calibration process in future.

The uncertainty on the tip curve could be improved by better understanding of the effects of exposing sidelobes to contrasting scenes, as the beam efficiency term dominates the error budget. It may be possible to devise an experiment to repeat tip curves over a greater range of elevation angles and examine the residuals of the measured brightness temperature from theory. The absolute level of this bias could also be reduced by redesigning the radiometer's quasi optics to avoid beam truncation above the -20 dB power level. This should improve the sidelobes, and reduce the magnitude of this term, and hence its' uncertainty.

This analysis has not included the real drift in T_{ND} between calibrations. This is the subject of future research! But it is clear that this will have more impact on the liquid nitrogen calibrations, which can only be performed infrequently.

These results also make a clear case to implement the tip curve calibration at the lowest frequency oxygen channel (51.25 GHz) if the random errors can be reduced by improving the estimation of the mean radiative temperature.

6. Observed v Modelled Brightness Temperatures in Clear Air

An independent validation of the radiometer's performance can be achieved by comparison of the observed brightness temperatures against modelled values. The radiative transfer model uses temperature and humidity profiles from radiosondes launched from the same site as the radiometer. This comparison is restricted to only those cases when the model can be trusted. The greatest uncertainty in the radiative transfer modelling is predicting the extinction due to clouds and precipitation. Providing 'ground truth' of these parameters for input to the models requires the use of empirical parameterizations, which introduce additional uncertainty in any comparison. For these reasons, the comparison is first done in clear sky conditions.

Radiative Transfer Models of Clear Air Absorption

At microwave and millimetre wavelengths, atmospheric absorption in clear air is dominated by oxygen and water vapour. Oxygen produces strong resonant absorption due to magnetic dipole rotational transitions at multiple frequencies in a band around 60 GHz and a single line at 118 GHz. Similarly, rotational transitions of the electric dipole of water vapour produce resonant absorption lines extending from the microwave to sub-millimetre wavelengths, including 22 GHz and 183 GHz. Typical emission spectra in clear air are shown in Figure 7.

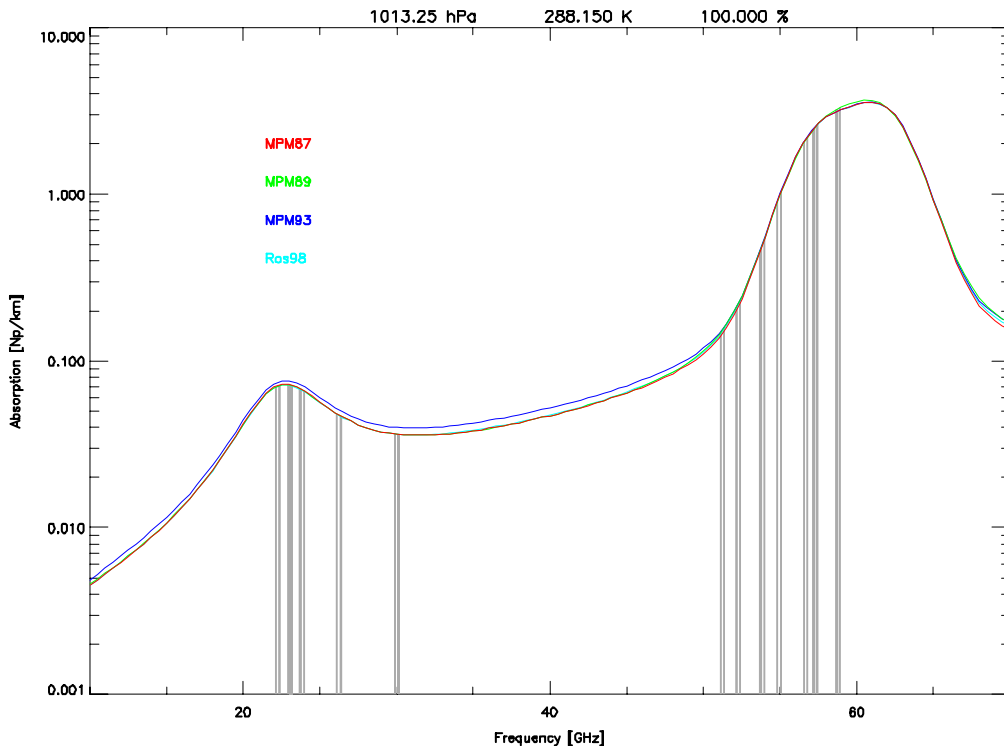


Figure 7 - Absorption in Clear Air from various Radiative Transfer Models at 1013.25 hPa, +15 °C, 100%RH

Between these absorption lines, the microwave spectrum is dominated by non-resonant emission from water vapour. Although many theories have been developed to explain the process responsible for the water vapour continuum, it is usually represented as an empirical term added to the theoretically based resonant terms to fit observations. It is generally divided into two contributions, which are self- and foreign- broadened, due to collisions of water vapour molecules with molecules of the same species or other gases, respectively.

There are also a small non-resonant contribution from dry air, including pressure-induced nitrogen absorption, which is small above 100 GHz, and oxygen, which is only significant below 10 GHz. Although the strength of these terms vary between the models, their impact is small. The differences between the models pertinent to this study are discussed in the following sub-sections. A more general discussion is given in Rayer [2001].

MPM87

The 'Original' Millimeter-wave Propagation Model [Liebe and Layton, 1987] used 44 oxygen and 30 water vapour lines to represent the absorption in clear air. This is supplemented by an empirically derived water vapour continuum, fitted to observations at 138 GHz. It added non-resonant emission due to dry air (oxygen and nitrogen). These are negligible in our case.

MPM89

The clear air absorption part of Liebe's Millimeter-wave Propagation Model, MPM89 [Liebe, 1989] includes 30 water vapour lines and 44 oxygen lines all in the range 20 GHz – 1 THz. Although it is based on MPM87, some of the line parameters have been modified. In particular, the parameters describing the 183 GHz water vapour line are based on observations, rather than theory. Additional terms represent the non-resonant absorption due to the Debye spectrum of oxygen below 10 GHz and the pressure-induced nitrogen absorption above 100 GHz. MPM89 provides the basis for the fast model ("RTTOV") used in the operational processing of AMSU data at the Met Office.

MPM93

This version of Liebe's Millimeter-wave Propagation Model [Liebe, 1993], has 34 water vapour lines between 20 GHz – 1 THz, defined in a slightly different manner from MPM89. The 183 GHz line is 8.5% wider and 5% stronger than in MPM89. The self-broadened part of the continuum absorption is formulated as a pseudo line at 1780 GHz. The foreign-broadened part of the continuum is fitted to newer observations.

Like its predecessor, MPM93 includes 44 oxygen lines with the same line strengths, but 5% greater widths and 15% stronger mixing than MPM89. Values used are based on updated measurements published in [Liebe et al., 1992]. The non-resonant nitrogen absorption is essentially the same as MPM89 at the frequencies in this study.

Rosenkranz'98

[Rosenkranz, 1998] uses 15 water vapour line parameters, which are very similar to the strongest lines used in MPM89. The other half of the line parameters have been omitted as they were found to have negligible impact. His investigations revealed a range of observations could be best modelled by using a water vapour continuum with a combination of MPM89's foreign-broadened component, and MPM93's self-broadened component. However, the water vapour lines used were truncated at ± 750 GHz, and the continuum adjusted to compensate. This model uses the same oxygen line parameters as MPM92 [Liebe *et al.*, 1992], except at sub-millimetre frequencies, where values from the HITRAN [Rothman *et al.*, 1992] database were used. It also uses a different form of non-resonant absorption due to pressure broadening by nitrogen, although this has a negligible impact at the frequencies used in this study.

The water vapour component of this model is used to train the neural network retrieval coefficients and is used to derive statistics used for this study. The oxygen component is taken from Rosenkranz, 1988, which is similar to MPM89.

Procedure

To minimise the uncertainty in the modelled brightness temperatures, the cases were selected thus:

- Use high-resolution radiosonde profiles from Camborne.
- 'Top-up' these profiles with a climatological profile above the burst point ~30 km.
- Only use data measured within one observation period of the launch of a radiosonde.
- Only use radiosondes where the observer reported $\leq 1/8$ low cloud.
- Only use radiometer data that is not flagged as 'Rain'.
- Only use radiometer data where the infrared brightness temperature, $T_{ir} \leq -40$ °C.

High resolution profiles of temperature and humidity (“2 second data”) are used as input to the radiative transfer models to minimise any errors introduced by layering the data. Radiosondes from Camborne are launched on 1200 g balloons, and typically reach altitudes of >30 km (~10 hPa). However, there is still a finite emission from atmosphere above this altitude, so the radiosonde profiles are ‘topped-up’ with a standard atmosphere (McCluthey mid-latitude winter). The choice of top-up profile causes a small, insignificant difference only for the 22.235 GHz channel.

For speed, the radiative transfer models are run at a single frequency to represent each channel. These frequencies were selected to produce zenith brightness temperatures that most closely matched the average of a comb of 22 frequencies spread over the passband of each channel. This tuning was repeated for 12 profiles, ranging from cold and dry to warm and humid. The models run at the *effective monochromatic frequency* agreed with an r.m.s. difference of <0.05 K of the full comb. The frequencies used are given in Table 21.

Results for Software v2.14

The radiometer was operated using software v2.14 for conditions covering almost a full annual cycle, from 22/3/2002 to 3/3/2003. During this period, there were 145 cases of coincident radiosonde and radiometer data in clear skies, meeting the above criteria. For each case, the observed brightness temperature closest to the radiosonde launch time was compared with 4 radiative transfer models. The difference (observed-modelled) is plotted against observed brightness temperature using a different colour for each model in Figure 8.

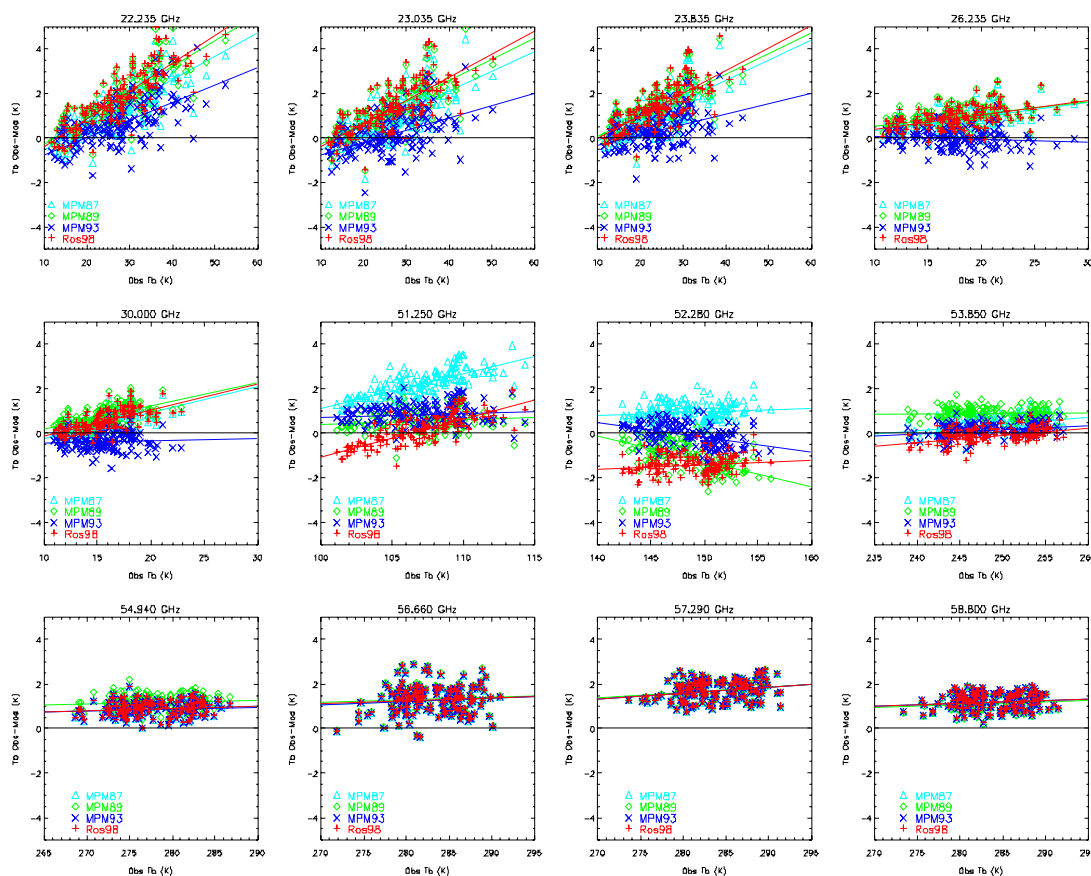


Figure 8 - Bias in Observations with respect to forward model based on 145 radiosondes with $\leq 1/8$ low cloud. Period 22/2/02 – 3/2/03. Software v2.14

The lowest frequency channels show a strong slope, with all models showing a significant bias in humid conditions. The RS80H radiosondes used at Camborne are known to have a dry bias due to sensor contamination and solar heating. The average maximum relative humidity measured in low cloud during this period was 97.0 %RH. If the profiles input to the radiative transfer model are corrected by increasing the vapour pressure by a factor of 1.03,

the difference between observations and model decreases, but a positive bias remains for all models. MPM93 then remains the closest model to the observations, although it overestimates the strength of the water vapour continuum at 26 – 30 GHz.

There is a consistent positive bias of 1 – 2 K at the highest frequencies due to the bias in the radiometer, discussed in Section 4. The channels in the wings of the oxygen complex (30 – 50 GHz) show substantial differences between the models, where MPM93 provides the best fit to the observations.

Table 21 – Statistics of Brightness Temperatures with respect to Radiative Transfer Models based on 145 radiosondes with $\leq 1/8$ low cloud. 22/2/02 – 3/2/03. Software v2.14

Effective Monochromatic Frequency (GHz)	Average Bias (Observations-Model) (K)				Standard Deviation (K)	r.m.s. (K)
	Δ MPM87	\diamond MPM89	\times MPM93	$+$ Ros98		
22.180	1.39	1.81	0.72	1.92	1.30	0.74
23.045	0.99	1.35	0.23	1.43	1.12	0.73
23.835	1.19	1.44	0.36	1.48	0.94	0.64
26.231	0.83	1.00	0.01	0.93	0.51	0.43
30.001	0.48	0.78	-0.35	0.57	0.46	0.35
51.256	2.25	0.57	0.91	0.18	0.66	0.44
52.288	0.98	-1.08	-0.08	-1.39	0.42	0.41
53.855	0.43	0.90	0.16	-0.08	0.33	0.30
54.934	0.92	1.21	0.89	0.94	0.33	0.35
56.655	1.30	1.36	1.29	1.31	0.64	0.63
57.287	1.72	1.76	1.72	1.74	0.44	0.42
58.804	1.23	1.18	1.22	1.24	0.37	0.37

The average bias, shown in Table 21 is significantly larger than that predicted in Table 20—in most cases by more than 2 standard uncertainties. This is evidence of a substantial bias that has not been accounted for in the analysis of Section 5. In the case of the lower frequency channels, this is believed to be a bias in the radiative transfer model, as these differ substantially in their predictions. The bias found in the radiometer explains most of the differences for the channels at 56 – 57 GHz.

Results for Software v2.20

Since upgrading the operating software to v2.20, there were fewer clear cases for validation of the observed brightness temperatures against modelled data. There have now been 36 cases with radiosondes launched in clear conditions, covering a broad range of conditions, including a trial at Cardington. The results are plotted in Figure 9. The Cardington data falls in the middle of the observed range, and produces generally consistent results with Camborne.

The water vapour channels give very consistent results with those obtained using v2.14: observations show a bias with respect to most models, which increases with higher humidity, which is partly explained by a dry bias in the radiosondes. MPM93 gives different results, and tends to overestimate brightness temperatures in high humidity after correcting the sondes.

The low frequency oxygen channels give similar results for both v2.14 and v2.20: large differences between models with MPM93 providing the best overall fit to the observations. The bias now appears to transition from low to high temperatures at 51.25 and 52.28GHz!

The high frequency oxygen channels show different results for the two software versions: The large positive bias of the observations with respect to all models found with v2.14 has been reduced at low temperatures, but is still found at higher temperatures. The cause of this should be investigated further. Overall the bias in these channels has reduced, as has the rms difference between the observations and model.

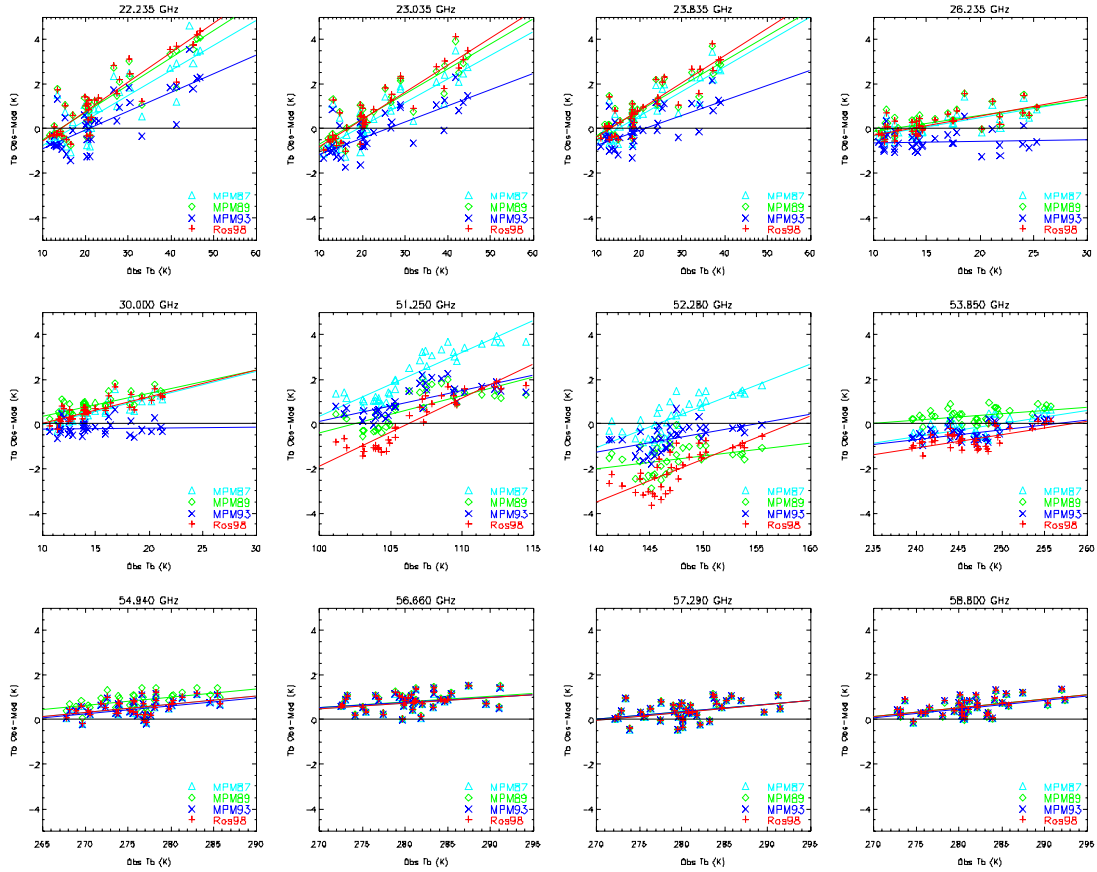


Figure 9 - Bias in Observations with respect to forward model based on 36 radiosondes with $\leq 1/8$ low cloud. Period 14/2/03 – 12/6/03. Software v2.20.

Random Noise Budget for Comparison of Observed and Modelled T_b

The comparison of measurements with forward modelled brightness temperatures provides valuable estimates of the random noise on the measurements (at least in clear sky conditions). Theoretically, the uncertainty on the observations—model difference is determined by the random noise on the radiometer measurements (including calibration noise), as well as that on the profile input to the model, plus any noise introduced by the model itself and additional terms to account for the representiveness of the profile and forecast errors.

$$\left[\epsilon(T_b^{OBS} - T_b^{MOD}) \right]^2 = E^2 + B^2 + F^2 + \left[\epsilon T_b^{REPRESENT} \right]^2 \tag{28}$$

where:

- $\epsilon(T_b^{OBS} - T_b^{MOD})$ is the r.m.s. difference between the observations and modelled T_b ,
- $E = \epsilon T_b^{OBS}$ is the uncertainty in the observations due to radiometer & calibration noise
- $B = \frac{dy\{x\}}{dx} \epsilon x$ is the uncertainty in the atmospheric state, x , propagated to brightness temperature, via the radiative transfer model, $y(x)$.
- F is the uncertainty in brightness temperature due to the random errors introduced by the forward model. It is assumed to be zero here.
- $\epsilon T_b^{REPRESENT}$ is the uncertainty in brightness temperature due to the errors of representiveness between the radiosonde's and radiometer's observations of the atmospheric state. Assumed to be zero here.

The Observation Error, E , is taken from random noise calculated in Table 13.

The forward model error, F , represents error introduced by the use of an effective monochromatic frequency. It is highest for the channel centred on the water vapour line, but also non-negligible for the channels in the wings of the oxygen complex. It is, however, a small contribution to the overall uncertainty.

The random error introduced by the sondes' sensors, B , is estimated by adding noise to each layer of the 1976 US standard atmosphere equivalent to the repeatability of the radiosondes' temperature and humidity sensors (± 0.2 K and $\pm 3\%$ RH). Ideally, the vertical covariance of the temperature and humidity should be used, but this was not available. It is assumed that the 40 layers of the standard atmosphere are independent in this respect. This process is repeated 1000 times to estimate the variance of the resulting brightness temperatures.

These terms are added in quadrature, the result, $(F^2+B^2+E^2)^{1/2}$ represents the total random noise expected on the difference between observations and model. However, this total is found to underestimate the r.m.s. difference of the comparison, shown in Table 21. Whilst this is the case for all channels, the difference is greatest for the channels with the greatest bias, and the causes are probably related. These figures are illustrated in Figure 10.

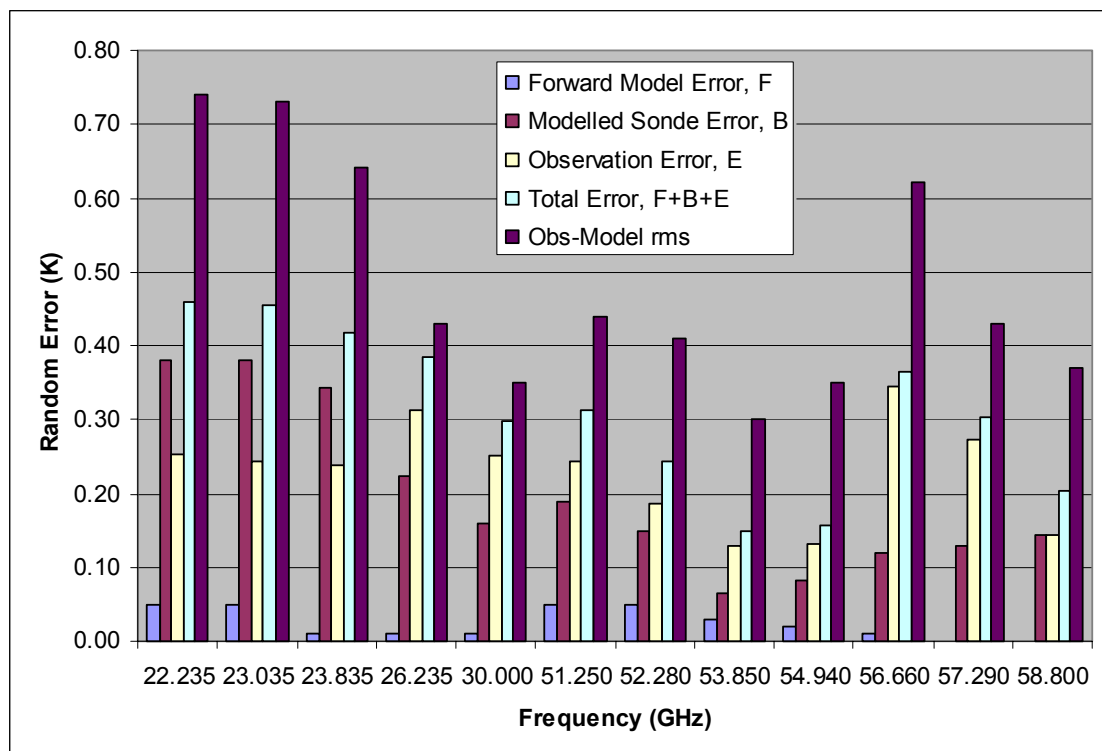


Figure 10 - Terms used to Estimate Random Error on Comparisons of Observed and Modelled Brightness Temperatures based on 138 radiosondes with $\leq 1/8$ low cloud. Period 22/2/02—3/2/03. Software v2.14

7. Conclusions and Recommendations

Radiometer noise is within specifications, which are adequate to retrieve some information on the structure of the lower troposphere. However, two channels are much noisier than the others. The cause of this should be investigated. Several modifications to the processing are suggested to further reduce the noise contribution from the calibration, especially noise that is correlated between different channels, as this will degrade the vertical resolution of retrievals.

Substantial biases were found in the brightness temperatures in both the oxygen band channels and the water vapour channels with comparison with forward modelled brightness temperatures. The biases in the oxygen channels have been reduced by a new release of the control software. The biases in the water vapour channels are found to be related to the total humidity, and are believed to be partly due to a bias in the forward model and partly due to the dry bias in the RS80H radiosonde sensors used during this trial.

Specific Recommendations for Radiometer Manufacturer

We recommend a complete over-haul of the structure of the archived data sets. This should follow the convention of Level 0 to include *all* raw data (e.g. voltages), Level 1 to include calibrated observations (e.g. brightness temperatures) and Level 2 to include derived products (e.g. retrieved profiles). These should be structured to allow the recreation of any data set from the previous level given a set of coefficients to represent the transform. This would greatly facilitate the analysis of the performance of the radiometer, its calibration and retrieval processes.

- Investigate cause of higher noise at 56.66 and 57.29 GHz.
- Test for standing waves by viewing a reflective plate.
- Investigate the effect of sidelobes on tip curve calibration.
- Investigate the loss introduced by polystyrene in the liquid nitrogen calibration.
- Confirm the magnitude of reflections from the liquid nitrogen-polystyrene interface.
- Include the measurement and correction for receiver non-linearity in the calibration.
- Average the radiometer gain and offset over longer period to reduce calibration noise.
- Improve the quality control and averaging of tip curve calibration data.
- Improve the estimation of mean radiative temperature used in tip curves.
- Investigate the application of tip curve calibration technique to channels near 50 GHz.
- Reduce the time difference between observations made by different channels.

Specific Recommendations for Upper Air Technology Centre

During the trial, we have formed an excellent working relationship with Radiometrics. We should continue liaison with them, while keeping abreast of developments from other manufacturers. Additionally, we should:

- Develop a non-stationary model to represent atmospheric variation and radiometer drift. This will allow a quantitative trade-off in specifying the optimum observation and calibration strategy. This has already been actioned and included in this revision of the report.

8. References

- J.Eyre, 1991:** "[Inversion methods for satellite sound data.](#)" Meteorological Training Course Lecture Series, ECMWF.
- Y.Han and E.R.Westwater, 2000:** "Analysis And Improvement Of Tipping Calibration For Ground-Based Microwave Radiometers," IEEE-TGARS, Vol.38, No.3, 2000, pp.1260-1276.
- T.J.Hewison and A.J.McGrath 2001:** "Performance assessment of Liquid Nitrogen Calibration Target supplied by Fred Solheim (Radiometrics) at 89, 157 and 183 GHz," MRF Technical Note 39, 2001. Available from National Meteorological Library, Met Office, UK.
- C.Gaffard and T.J.Hewison, 2003:** "Radiometrics MP3000 Microwave Radiometer Trial Report", Met Office (OD) Technical Report 26, from National Meteorological Library, UK.
- M.A.Janssen, 1993:** "Atmospheric remote sensing by microwave radiometry," Wiley Series in Remote Sensing.
- James W. Lamb, 1996:** "Miscellaneous Data On Materials For Millimetre And Submillimetre Optics," Int. J. IR and Millimeter Waves, vol. 17, no. 12, pp.1997-2034, Dec. 1996.
- Liebe, H.J and D.H.Layton, 1987:** "Millimeter-Wave Properties Of The Atmosphere: Laboratory Studies And Propagation Modeling", NTIA-Report 87-224, Natl. Telecommun. And Inf. Admin, Boulder, CO.
- Liebe, H.J., 1989:** "MPM - An Atmospheric Millimeter Wave Propagation Model, Int. J. Infrared and Millimeter Waves", Vol.10(6), pp.631-650.
- Liebe, H.J., P.W.Rosenkranz and G.A.Hufford, 1992:** "Atmospheric 60-Ghz Oxygen Spectrum: New Laboratory Measurements And Line Parameters", J. Quant. Spectrosc. Radiat. Transfer, Vol.45, No.5/6, pp.629-643, 1992.
- Liebe, H.J., G.A.Hufford and M.G.Cotton, 1993:** Propagation modeling of moist air and suspended water/ice particles at frequencies below 1000GHz, AGARD 52nd Specialists' Meeting of the Electromagnetic Wave Propagation Panel, Ch3.
- McGrath, A.J. and T.J.Hewison, 2001:** "Measuring the accuracy of a Microwave Airborne Radiometer (MARSS)", Journal of Atmospheric and Oceanographic Technologies, Vol.18, No.12, 2001, pp.2003-2012
- Radiometrics, 2001:** "TP/WVP-3000 Temperature and Water Vapor Profiling Radiometer" Operators handbook. Radiometrics Corporation, <http://radiometrics.com>.
- Rayer, P.J. 2001:** "[Microwave transmittance models for RTTOV, EUMETSAT NWP SAF Deliverable 8.1](#)", 2001, available online from <http://www.metoffice.com/>.
- Rosenkranz, P.W., 1998:** "Water Vapor Microwave Continuum Absorption: A Comparison Of Measurements And Models", Radio Science, Vol.33, No.4, pp.919-928.
- Rothman, L.S, et al., 1992:** "The HITRAN molecular database: Editions of 1991 and 1992," J. Quant. Spectrosc. Radiat. Transfer, 48, pp.469-507.
- Sanford, J., 1995:** "A Luneberg lens update," IEEE Antennas and Propagation, Vol.37, No.1, pp.76-69, Feb 1995.
- Solheim, F., J. Godwin, and R. Ware, 1996:** "[Microwave Radiometer for Passively and Remotely Measuring Atmospheric Temperature, Water Vapor, and Cloud Liquid Water Profiles](#)", *Final Contract Report DAAL01-96-2009, White Sands Missile Range*.
- Wilks, Daniel S. , 1995:** "Statistical Methods in the Atmospheric Sciences," Academic Press.
- Ulaby, F.T., R.K.Moore and A.K.Fung, 1981:** "Microwave Remote Sensing - Active and Passive, Volume I: Microwave Remote Sensing Fundamentals and Radiometry," Reading, MA: Addison-Wesley.
- Vinogradov, E.A., E.M.Dianov and N.A.Irisova, 1967:** "Dielectric characteristics of liquid nitrogen at $\lambda=2.3\text{mm}$," Soviet Physics - Technical Physics, Vol.11, No.7, 1967, p.983.